Petroleum Science 21 (2024) 143–161

Contents lists available at ScienceDirect

Petroleum Science

journal homepage: www.keaipublishing.com/en/journals/petroleum-science

Original Paper

P- and SV-wave dispersion and attenuation in saturated microcracked porous rock with aligned penny-shaped fractures

Sheng-Qing Li [a, b], Wen-Hao Wang [a], Yuan-Da Su [a, b], Jun-Xin Guo [c, d, *], Xiao-Ming Tang [a, b]

[a] School of Geosciences, China University of Petroleum (East China), Qingdao 266580, Shandong, China
[b] Laoshan National Laboratory, Qingdao 266071, Shangdong, China
[c] Guangdong Provincial Key Laboratory of Geophysical High-resolution Imaging Technology, Southern University of Science and Technology, Shenzhen 518055, Guangdong, China
[d] Department of Earth and Space Sciences, Southern University of Science and Technology, Shenzhen 518055, Guangdong, China

ARTICLE INFO

Article history:
Received 12 December 2022
Received in revised form
11 May 2023
Accepted 25 August 2023
Available online 26 August 2023

Edited by Jie Hao

Keywords:
Aligned fractures
P- and SV-wave
Dispersion and attenuation
Microcracked porous background
FB-WIFF
Elastic scattering
Squirt flow

ABSTRACT

P- and SV-wave dispersion and attenuation have been extensively investigated in saturated poroelastic media with aligned fractures. However, there are few existing models that incorporate the multiple wave attenuation mechanisms from the microscopic scale to the macroscopic scale. Hence, in this work, we developed a unified model to incorporate the wave attenuation mechanisms at different scales, which includes the microscopic squirt flow between the microcracks and pores, the mesoscopic wave-induced fluid flow between fractures and background (FB-WIFF), and the macroscopic Biot's global flow and elastic scattering (ES) from the fractures. Using Tang's modified Biot's theory and the mixed-boundary conditions, we derived the exact frequency-dependent solutions of the scattering problem for a single penny-shaped fracture with oblique incident P- and SV- waves. We then developed theoretical models for a set of aligned fractures and randomly oriented fractures using the Foldy approximation. The results indicated that microcrack squirt flow considerably influences the dispersion and attenuation of P- and SV-wave velocities. The coupling effects of microcrack squirt flow with the FB-WIFF and ES of fractures cause much higher velocity dispersion and attenuation for P waves than for SV waves. Randomly oriented fractures substantially reduce the attenuation caused by the FB-WIFF and ES, particularly for the ES attenuation of SV waves. Through a comparison with existing models in the limiting cases and previous experimental measurements, we validated our model.

1. Introduction

A rock fracture is a mechanical break or discontinuity that divides a rock mass into two or more parts (Jiang et al., 2009; Shang et al., 2018). Loss of continuity or cohesion of a rock mass at the fracture seriously affects the mechanical and hydraulic properties of the rock. More specifically, when the applied stress reaches a certain limit, rock fractures form, which are accompanied by a number of microcracks (Walsh, 1965; Kuster and Toksöz, 1974; Ivars et al., 2011; Gudmundsson, 2011). These reduce the elasticity of the rock and provide additional reservoir space and fluid flow conduits for oil and gas, especially for unconventional reservoirs, such as carbonate and unconventional tight gas, shale gas, and coal reservoirs (e.g., Engelder et al., 2009; Liu et al., 2017a; Golsanami et al., 2019).

Because the resolution of seismic detection is low when imaging individual fractures, seismic attributes are often used for fracture detection and characterization (Baird et al., 2013). When a seismic wave propagates in a saturated cracked porous rock, many attenuation phenomena occur (Johnston et al., 1979), such as fluid compression in the fracture, fluid extrusion from the microcracks (or soft pores) to stiff pores, and friction loss of the fluid with respect to the solid in the pore space. Wave-induced fluid flow (WIFF) between fractures and a porous background (FB-WIFF) often occurs at low frequencies (Hudson, 1981; Galvin and Gurevich, 2009); microcrack squirt flow is mainly determined by the compliance crack (or soft pore) aspect ratio (O'Connell and

* Corresponding author. Guangdong Provincial Key Laboratory of Geophysical High-resolution Imaging Technology, Southern University of Science and Technology, Shenzhen, Guangzhou, 518055, China.
E-mail address: guojx@sustech.edu.cn (J.-X. Guo).

https://doi.org/10.1016/j.petsci.2023.08.029

Budiansky, 1977; Dvorkin et al., 1995; Gurevich et al., 2010; Adelinet et al., 2011; Tang et al., 2012). In addition to WIFF, wave elastic scattering (ES) by the fracture surface is notable when the size of the fracture is comparable to the wavelength (Gurevich et al., 1997; Galvin and Gurevich, 2007, 2009; Sato et al., 2012; Guo et al., 2018c), especially for large, macroscale fractures.

Many theories have been developed for studying wave propagation in jointed rock masses. These theories can generally be divided into two categories. One category involves studying the effects of fractures on wave propagation. For this purpose, most of the models have been proposed to discuss the FB-WIFF (Galvin and Gurevich, 2009; Fu et al., 2018; Guo et al., 2018a, 2018b) and the coupling effect of the FB-WIFF and ES (Fu et al., 2020; Guo and Gurevich, 2020a, 2020b). Guo et al. (2022a, 2022b) studied wave-induced fluid flow between intersecting fractures (FF-WIFF) and their coupling effects with FB-WIFF and ES. The second category involves studying the effects of microcracks on wave propagation. As reported by Dvorkin and Nur (1993), the considerable wave velocity dispersion and attenuation observed in rock velocity measurements are not well-described by Biot theory. This is because of the assumption that the pore space is uniformly distributed, which ignores the effects of local flow on the elastic properties of the rock at the pore scale. To overcome this defect, Berryman and Wang (1995), Pride and Berryman (2003a, 2003b), and Berryman (2006) developed the theory of dual-pore media. In dual-porosity media theory, local flow is controlled by the pore structure and the fluid pressure difference between the two types of pores. Based on the Biot-Consistent theory (Thomsen, 1985), Tang et al. (2012) extended the Biot theory to pore–microcrack coexisting media and added microcrack density and microcrack aspect ratio parameters to consider the effects of microcracks. In their theory, microcracks are randomly oriented, and the squirt flow effect is dominant, producing large wave velocity dispersion and attenuation for interpreting observed sonic logging data (Chen et al., 2014; Markova et al., 2014). However, this mechanism cannot explain the attenuation observed in seismic frequency bands (Pride et al., 2004). In addition, according to Ma and Ba (2020), intrinsic attenuation in tight siltstones is mainly caused by WIFF between microcracks and intergranular pores. Furthermore, Zhang et al. (2021, 2022) investigated the WIFF at different scales and partial saturation in the fractal texture of porous media based on the differential effective medium and the Biot-Rayleigh theories. Deng and Morozov (2019, 2020) construct a general model that accounts for macroscopic local deformation effects through Lagrangian continuum mechanics.

In this study, we developed a theoretical model to describe the dispersion and attenuation of oblique incident P and SV waves, where the rock background contains both stiff pores and compressible microcracks, and the macroscale fractures are sparsely distributed in the background. The case with aligned macroscale fractures was studied, as well as that with random orientation. We investigated the attenuation mechanisms of FB-WIFF, ES, microcrack squirt flow, and Biot flow and their coupling effects. First, we derived generalized solution expressions for the scattered wavefields in a saturated microcracked porous medium. Then, the solution coefficients of the scattered wavefields were obtained according to the mixed-boundary conditions of a single fracture. Finally, according to the far-field Foldy approximation of scattered wavefields, the complex effective P and SV wavenumbers were obtained. To verify our model, we compared our model predictions with existing models for limiting cases and with the previous experimental measurements reported by Tillotson et al. (2014).

2. Theoretical background

We considered plane, time-harmonic P- and SV-wave propagating in a saturated microcracked porous rock, which contained aligned penny-shaped fractures (Fig. 1a). It was assumed that fractures were randomly and sparsely distributed in the medium. Using Tang's poroelastic equations for pore–microcrack coexisting media (Tang et al., 2012), we investigated the scattered wavefields of oblique incident P- and SV-wave in a fluid-saturated microcracked porous medium.

2.1. Modified wave motion equations in a saturated microcracked porous medium

Based on the Lagrange equations of a complicated force system, Biot (1962) established the dynamic elastic wave propagation equations of a fluid-filled porous medium as follows:

$$-\nabla\cdot\boldsymbol{\sigma} = \omega^2\left(\rho\mathbf{u_s} + \rho_f\mathbf{w}\right), \tag{1}$$

$$\nabla p_f = \omega^2\left(\rho_f\mathbf{u_s} + \rho'\mathbf{w}\right). \tag{2}$$

where ω denotes the angular frequency; $\boldsymbol{\sigma}$ denotes the total stress tensor and p_f denotes the pressure of pore fluid; $\mathbf{w} = \varphi(\mathbf{u_f} - \mathbf{u_s})$ is the fluid displacements relative to the solid; φ represents the porosity; $\mathbf{u_f}$ and $\mathbf{u_s}$ represent the displacements of the solid and pore fluid, respectively; $\rho = (1-\varphi)\rho_s + \varphi\rho_f$ represents the density of the overall rock, with ρ_s and ρ_f being the densities of the solid phase and pore fluid, respectively; $\rho' = i\eta/\omega\kappa(\omega)$ is called the effective filtration density; η represents the fluid viscosity; $\kappa(\omega) = \kappa_0\left[\sqrt{1 - \frac{i\omega\kappa_0\alpha_\infty\rho_f}{2\varphi\eta}} - \frac{i\omega\kappa_0\alpha_\infty\rho_f}{\varphi\eta}\right]^{-1}$ is Johnson et al. (1987) dynamic permeability, where κ_0 is the static Darcy permeability, and α_∞ is the tortuosity.

Biot and Willis (1957) derived the constitutive relationships between the displacements and average stress tensor as follows:

$$\boldsymbol{\sigma} = [(H-2\mu)\nabla\cdot\mathbf{u_s} + C\nabla\cdot\mathbf{w}]\mathbf{I_2} + \mu[\nabla\cdot\mathbf{u_s} + \mathbf{u_s}\nabla], \tag{3}$$

$$-p = C\nabla\cdot\mathbf{u_s} + M\nabla\cdot\mathbf{w}. \tag{4}$$

where $\mathbf{I_2}$ is the Kronecker tensor; μ is the dry shear modulus of the porous medium; $M = \left[(\alpha-\varphi)/K_s + \varphi/K_f\right]^{-1}$ is the Biot fluid storage modulus; $\alpha = 1 - K_d/K_s$ is the Biot–Willis parameter, where K_d and K_s are the bulk moduli of the dry porous medium and solid phase, respectively; K_f is the bulk modulus of pore fluid; $H = K_d + 4\mu/3 + \alpha^2 M$ is the P-wave modulus of saturated porous rock at low frequency, and modulus $C = \alpha M$.

To describe the wave-induced fluid flow of microscale cracks, Tang et al. (2012) considered the wave-induced squirt flow between microcracks (or soft pores) and pore space. The constitutive equations were rewritten as:

$$\sigma_{ij} = 2\mu e_{ij} + \left[(K_d - 2\mu/3)e - \alpha p_f\right]\delta_{ij}, \tag{5}$$

$$-p_f = \widehat{C}\nabla\cdot\mathbf{u_s} + \widehat{M}\nabla\cdot\mathbf{w}, \tag{6}$$

where e_{ij} is the Cauchy strain tensor and $e = \nabla\cdot\mathbf{u_s}$; δ_{ij} is the Kronecker delta; K_d is the dry bulk modulus of microcracked

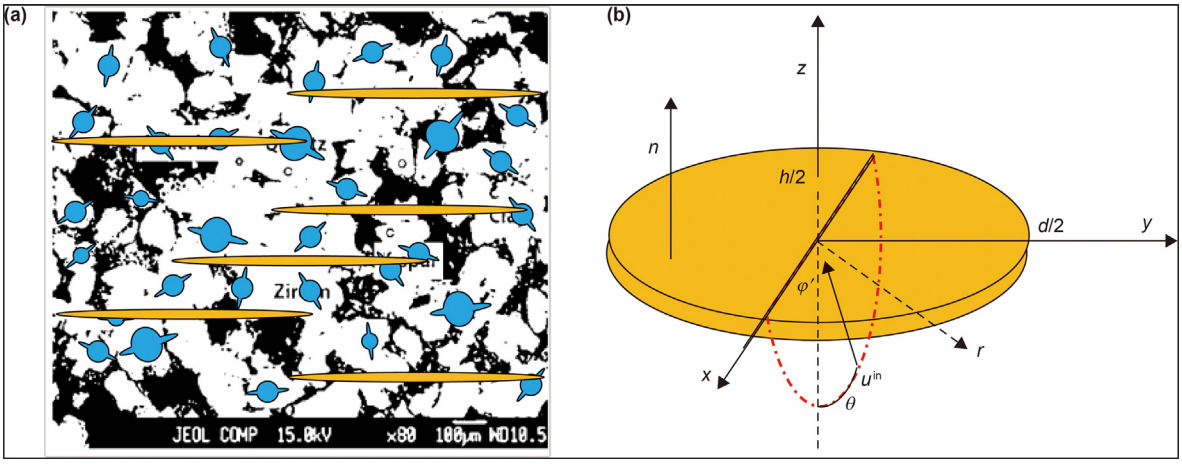

Fig. 1. (a) Saturated isotropic rock matrix containing a set of randomly oriented cymbal-shaped pore-microcrack structures (microscopic scale) and aligned penny-shaped fractures (macroscopic scale); (b) P- or SV- wave oblique incidence into a penny-shaped fracture center plane, where **n** refers to the fracture normal, d refers to the fracture diameter, and h refers to the fracture thickness. The wave incident on the x-z plane with $\varphi' = 0$, and θ refers to the wave incidence angle relative to the z-axis.

background; and $\widehat{C} = \alpha\widehat{M}$, where $\widehat{M} = [M^{-1} + S(\omega)]^{-1}$, with the squirting function $S(\omega)$ given by:

$$S(\omega) = \frac{8\varepsilon_{\mathrm{mic}}(1-\nu_0)(1+\lambda)^3 N(1/K_0 - 1/K_s)\Big/[3\mu_0(1/K_d - 1/K_0)]}{1 - \frac{3i\omega\eta(1+2\lambda)}{2K_f\lambda\gamma_{\mathrm{mic}}^2}\left[1 + \frac{4(1-\nu_0)K_f(1+\lambda)^3}{3\pi\mu_0\gamma_{\mathrm{mic}}(1+2\lambda)}N\right]}. \tag{7}$$

where $N = 1 + \lambda^3\frac{4-5\nu_0}{(14-10\nu_0)(1+\lambda)^3} + \lambda^5\frac{9}{(14-10\nu_0)(1+\lambda)^5}$; $\lambda = \left(\frac{3\varphi}{4\pi\varepsilon_{\mathrm{mic}}}\right)^{1/3}$ is the pore-to-microcrack size ratio; $\varepsilon_{\mathrm{mic}}$ is the microcrack density; γ_{mic} is the microcrack aspect ratio; μ_0, K_0, and ν_0 are the shear modulus, bulk modulus, and Poisson's ratio of the microcracked rock background (frame) without considering the squirt flow, respectively.

When the microcrack density and (or) microcrack aspect ratio changes, the modulus K_d, μ_0, K_0 and Poisson's ratio ν_0 in Eq. (7) will also change. According to the Biot-Consistent theory (Thomsen, 1985), these parameters can be obtained as a function of microcrack density and rock porosity (the details are given in Appendix A):

$$\begin{aligned} &K_d = K_d(\varepsilon_{\mathrm{mic}}, \varphi), \mu_0 = \mu_0(\varepsilon_{\mathrm{mic}}, \varphi), K_0 = K_0(\varepsilon_{\mathrm{mic}}, \varphi), \\ &\nu_0 = \nu_0(\varepsilon_{\mathrm{mic}}, \varphi), \end{aligned} \tag{8}$$

Hence, the saturated bulk and frame shear moduli of a microcracked porous medium can be derived using the procedure reported by Tang et al. (2012), as follows:

$$K = K_d + \alpha^2\widehat{M}, \tag{9}$$

$$\mu = \left[4\left(K^{-1} - K_0^{-1}\right)\Big/15 + \mu_0^{-1}\right]^{-1}. \tag{10}$$

More specifically, first, the modulus K_d and μ_0 can be obtained from Eq. (8) through the Biot-Consistent condition (Thomsen, 1985). And then, the modulus K_0 is calculated from Eq. (9) by setting the squirt function $S(\omega) = 0$ in the modulus $\widehat{M}$ [Eq. (A14)]. The Poisson's ratio ν_0 can be determined from the relationship with K_0 and μ_0 [Eq. (A15)].

Note that the squirting function $S(\omega)$ does not approach zero at the low-frequency limit. Thus, the saturated bulk modulus calculated using Eq. (9) does not satisfy the Gassmann limit (Yao et al., 2015; Zhang et al., 2019). Therefore, we modified the saturated bulk modulus K^m as follows (Wang and Tang, 2021):

$$K^m = K_d + \alpha^2 M + [K - K(0)]. \tag{11}$$

where $K(0)$ is the bulk modulus calculated using Eq. (9), with a squirting function at zero frequency. Replacing K with K^m in Eq. (10) yields the modified frame shear modulus.

From Eq. (5), we rewrote the average stress tensor constitutive equation in its equivalent form, as follows:

$$\boldsymbol{\sigma} = (K_d - 2\mu/3)\nabla\cdot\mathbf{u_s}\mathbf{I_2} + \mu[\nabla\cdot\mathbf{u_s} + \mathbf{u_s}\nabla] - \alpha p_f\mathbf{I_2}, \tag{12}$$

Then, substituting Eq. (6) into (12) and simplifying to a form similar to Eq. (3) as:

$$\boldsymbol{\sigma} = [(\widehat{H} - 2\mu)\nabla\cdot\mathbf{u_s} + \widehat{C}\nabla\cdot\mathbf{w}]\mathbf{I_2} + \mu[\nabla\cdot\mathbf{u_s} + \mathbf{u_s}\nabla]. \tag{13}$$

where $\widehat{H} = K^m + 4\mu/3$ is the P-wave modulus of the saturated microcracked porous medium.

2.2. Oblique incident P and SV waves

In this work, the cymbal-shaped pore-microcrack structures are at the microscopic scale, while the aligned fractures considered are at the macroscopic scale. As each individual fracture is rotationally symmetric about its normal, as shown in Fig. 1b, we have established a cylindrical coordinate system (r, φ', z). The center of the system coincides with the center of the fracture, and the P- or SV-wave is incident on the x-z plane ($\varphi' = 0$). When the P- or SV-wave is obliquely incident, the incident wave displacement (omit time harmonic factor $e^{-i\omega t}$) can be expressed as:

$$\begin{cases} \mathbf{u_p^{in}} = u_0(\sin\theta, \cos\theta)e^{ik_1 x\sin\theta + ik_1 z\cos\theta} \\ \mathbf{u_{sv}^{in}} = u_0(\cos\theta, -\sin\theta)e^{ik_3 x\sin\theta + ik_3 z\cos\theta} \end{cases}. \tag{14}$$

where u_0 is the displacement amplitude, θ is the wave incidence angle relative to the fracture normal **n** (along the z-axis), and k_1 and k_3 represent the complex fast P- and SV- wavenumbers, respectively.

2.3. Solutions for single fracture scattered wavefields

Using the elastic wave propagation equations (Eqs. (1) and (2)) and the constitutive equations (Eqs. (6) and (13)) in a microcracked porous medium, we obtained the general solutions for the scattered wavefields from a single fracture similar to those proposed by Song (2017). The difference is that we replaced the moduli in the constitutive equations given by Biot theory (Eqs. (3) and (4)) with the effective moduli, taking into account the microcrack squirt-flow effects (Eqs. (6) and (13)). For simplicity, the general solutions are given in Appendix B. Since the form of the constitutive equations remains unchanged, the general solutions have identical forms.

2.4. Boundary conditions of a single fracture

As discussed by Song (2017) and Guo and Gurevich (2020b), the problem of wave obliquely incident fracture surface can be decomposed into two parts: the normal fracture discontinuity problem and the shear fracture discontinuity problem. The boundary conditions of both problems have been provided by Guo and Gurevich (2020a, 2020b), which we briefly introduce in the next section; a specific derivation can be found in Guo and Gurevich (2020a, 2020b).

2.4.1. Boundary conditions of the normal fracture discontinuity problem

Due to the symmetric discontinuity characteristics of the normal fracture discontinuity on the fracture center plane ($z = 0$), we studied the normal fracture discontinuity problem in the upper half space ($z > 0$). According to the upper half-space fracture surface boundary, we considered the boundary conditions of the scattered wavefields (a scattered wavefield is the difference between the total and incident wavefields) in the z-, r-, and φ'-axis directions (Guo and Gurevich, 2020a):

$$\sigma_{zr}^{m}\pm\sigma_{z\varphi}^{m}=0,\quad z=0,\quad 0\le r<\infty, \tag{15}$$

$$\sigma_{zz}^{m}+p_{\mathrm{f}}^{m}=-\left(\sigma_{zz}^{m,\mathrm{in}}+p_{\mathrm{f}}^{m,\mathrm{in}}\right),\quad z=0,\quad 0\le r\le d/2, \tag{16}$$

$$\begin{cases} u_z^m+w_z^m=-\dfrac{p_{\mathrm{f}}^m h}{2K_{\mathrm{f}}}, & z=0,\quad 0\le r\le d/2 \\ u_z^m+w_z^m=0, & z=0,\quad d/2\le r\le\infty, \end{cases} \tag{17}$$

$$u_z^m=0,\quad z=0,\quad d/2\le r\le\infty. \tag{18}$$

where the superscript "in" refers to the effects of incident waves; σ_{zr}^m and $\sigma_{z\varphi}^m$ represent the mth component of the scattered wavefields' radial shear stress and torsion stress, respectively; u_z^m and w_z^m are the mth component of the scattered solid displacement and relative fluid displacement in the z-axis direction, respectively; σ_{zz}^m and p_{f}^m represent the mth component of the scattered wavefields' normal stress and fluid pressure, respectively; and $\sigma_{zz}^{m,\mathrm{in}}$ and $p_{\mathrm{f}}^{m,\mathrm{in}}$ are those caused by incident waves, respectively.

2.4.2. Boundary conditions of the shear fracture discontinuity problem

For shear discontinuity on a fracture surface, the shear displacement on the positive z-axis is opposite to that on the negative z-axis. Hence, the boundary conditions of the shear fracture discontinuity problem were provided by Guo and Gurevich (2020b):

$$\sigma_{zr}^{m}\pm\sigma_{z\varphi}^{m}=-\left(\sigma_{zr}^{m,\mathrm{in}}\pm\sigma_{z\varphi}^{m,\mathrm{in}}\right),\quad z=0,\quad 0\le r<d/2, \tag{19}$$

$$u_r^m\pm u_\varphi^m=0,\quad z=0,\quad d/2\le r<\infty, \tag{20}$$

$$\sigma_{zz}^m=p_{\mathrm{f}}^m=0,\quad z=0,\quad 0\le r<\infty. \tag{21}$$

where $\sigma_{zr}^{m,\mathrm{in}}$ and $\sigma_{z\varphi}^{m,\mathrm{in}}$ represent the mth component of the radial shear stress and torsion stress induced by the incident wave, respectively; u_r^m and u_φ^m refer to the solid displacements of the mth component of the scattering wave fields in the r- and φ'-axis directions, respectively.

2.5. Solution of scattered wavefields coefficients by Fredholm integration

The next step involved obtaining the undetermined coefficients within the general solutions of the scattered wavefields that were consistent with the boundary conditions in Section 2.4. We used the above complex boundary conditions for the normal and shear fracture discontinuity problems to derive the coefficients.

2.5.1. Solutions for the normal fracture discontinuity problem

First, the general solutions Eqs. (B2–B4) are substituted into the boundary conditions in Eqs. (17) and (15), respectively, to obtain the relationship between the undetermined coefficients, which are expressed as follows:

$$C_n^m(\omega,k)=\frac{2\left[A_n^m(\omega,k)Q_1+B_n^m(\omega,k)Q_2\right]}{2k^2-k_3^2},\quad 0\le r<\infty, \tag{22}$$

$$B_n^m(\omega,k)=-\frac{G_1}{G_2}A_n^m(\omega,k),\quad 0\le r\le d/2, \tag{23}$$

$$B_n^m(\omega,k)=-\frac{2k^2(\chi_3-\chi_1)+k_3^2(1+\chi_1)}{2k^2(\chi_3-\chi_2)+k_3^2(1+\chi_2)}\frac{Q_1}{Q_2}A_n^m(\omega,k),\quad d/2<r<\infty, \tag{24}$$

where

$$G_i=2Q_iK_{\mathrm{f}}\left[2k^2(\chi_3-\chi_i)+k_3^2(1+\chi_i)\right]+hk_i^2(\widehat{C}+\widehat{M}\chi_i)\left(2k^2-k_3^2\right)\Big\},\quad i=1,2. \tag{25}$$

where the subscript "n" represents the case of normal fracture discontinuity. Subsequently, substituting the general solutions of Eqs. (B5), (B6) and (B2) into the boundary conditions in Eqs. (16) and (18) and using the relationships in Eqs. (22)–(24), the dual integrals for $A_n^m(\omega,k)$ can be obtained as follows:

$$\begin{cases} \displaystyle\int_0^\infty \frac{Q_1 kA_n^m(\omega,k)}{2k^2(\chi_3-\chi_2)+k_3^2(1+\chi_2)}J_m(kr)\mathrm{d}k=0, & d/2<r<\infty \\ \displaystyle\int_0^\infty \left[F_{n,1}(\omega,k)-F_{n,2}(\omega,k)\right]A_n^m(\omega,k)J_m(kr)k\mathrm{d}k=-f_n(\omega,r), & 0\le r\le d/2, \end{cases} \tag{26}$$

where

$$F_{n,i}(\omega,k)=\left\{2\mu k^2-[\widehat{H}-\widehat{C}+\chi_i(\widehat{C}-\widehat{M})]k_i^2-\frac{4\mu k^2Q_3Q_i}{2k^2-k_3^2}\right\}\cdot\left(\frac{G_1}{G_2}\right)^{i-1},\quad i=1,2, \tag{27}$$

where $f_n(\omega,r)$ can be determined by substituting Eq. (14) into the Eqs. (6) and (13) respectively.

Then, using the decomposition formula $e^{ik_ix}=\sum_{m=0}^{\infty}\upsilon_m i^m J_m(k_ir)\cos\varphi$, $(i=1,\ 3)$ and the relationship $\mathbf{w}=\chi_i\mathbf{u}_s$, $(i=1,\ 3)$, the function $f_n(\omega,r)$ in Eq. (26) for P- and SV-wave can be expressed as follows:

$$f_n^{\mathrm{p}}(\omega,r)=\upsilon_m i^{m+1}u_0k_1\left[\widehat{H}-\widehat{C}+\chi_1(\widehat{C}-\widehat{M})-2\mu\sin^2\theta\right]J_m(k_1r\sin\theta), \tag{28}$$

$$f_n^{\mathrm{sv}}(\omega,r)=-\upsilon_m i^{m+1}u_0\mu k_3\sin 2\theta J_m(k_3r\sin\theta). \tag{29}$$

where the superscripts P and SV denote the incidence of P- and SV-wave, respectively; υ_m denotes the Neumann factor, which is $\upsilon_m=1$ for $m=0$ and $\upsilon_m=2$ for $m>0$.

As discussed by Song et al. (2017), Eq. (26) can be rewritten in the form introduced by Noble (1963) as follows:

$$\begin{cases}\displaystyle\int_0^{\infty}U_n(\omega,k)J_m(kr)\mathrm{d}k=0, & d/2<r<\infty\\ \displaystyle\int_0^{\infty}[1+H_n(\omega,k)]U_n(\omega,k)J_m(kr)k\mathrm{d}k=-f_n(\omega,\theta), & 0\le r\le d/2,\end{cases} \tag{30}$$

where

$$U_n(\omega,k)=\frac{E_n(\omega)Q_1kA_n^m(\omega,k)}{2k^2(\chi_3-\chi_2)+k_3^2(1+\chi_2)}, \tag{31}$$

$$H_n(\omega,k)=E_n^{-1}(\omega)[F_{n1}(\omega,k)-F_{n2}(\omega,k)]\left[2k^2(\chi_3-\chi_2)+k_3^2(1+\chi_2)\right]Q_1^{-1}k^{-1}-1, \tag{32}$$

where $E_n(\omega)$ is required to ensure that $\lim_{k\to\infty}H_n(\omega,k)=0$ follows Noble's solution method (Noble, 1963), which can be expressed as:

$$E_n(\omega)=2\sum_{j=1}^{2}(-1)^j\left(\chi_3-\chi_2-\chi_1+\chi_j\right)\left[\widehat{H}-\widehat{C}+\chi_j(\widehat{C}-\widehat{M})\right]k_j^2. \tag{33}$$

Finally, the Fredholm integral of the second kind for solving coefficients $A_n^m(\omega,k)$ can be expressed as:

$$\Phi_n(\omega,\tau)+\int_0^{d/2}W_n(\omega,\tau,\tilde{\tau})\cdot\Phi_n(\omega,\tilde{\tau})\mathrm{d}\tilde{\tau}=F_n(\omega,\tau),\quad 0\le\tau\le d/2, \tag{34}$$

where

$$W_n(\omega,\tau,\tilde{\tau})=\sqrt{\tau\cdot\tilde{\tau}}\int_0^{\infty}H_n(\omega,k)J_{0.5+m}(k\tau)J_{0.5+m}(k\tilde{\tau})k\mathrm{d}k, \tag{35}$$

$$F_n(\omega,\tau)=-\frac{1}{\tau^m}\int_0^{\tau}\frac{f_n(\omega,r)r^{m+1}}{\sqrt{\tau^2-r^2}}\mathrm{d}r, \tag{36}$$

and

$$U_n(\omega,k)=\sqrt{\frac{2k}{\pi}}\int_0^{d/2}\sqrt{\tilde{\tau}}\Phi_n(\omega,\tilde{\tau})J_{0.5+m}(k\tilde{\tau})\mathrm{d}\tilde{\tau}. \tag{37}$$

The function $\Phi_n(\omega,\tilde{\tau})$ can be solved numerically, and the detailed numerical solution method of the second type of Fredholm integral is shown in Appendix D. Then, substituting the results into Eq. (37) and compared with Eq. (31), we can derive the solution for the scattered wavefield coefficient, $A_n^m(\omega,k)$. Finally, the coefficient $C_n^m(\omega,k)$ can then be obtained using Eqs. (22) and (24) for the normal fracture–discontinuity problem.

2.5.2. Solutions for the shear fracture discontinuity problem

The derivations of the shear scattering wavefield coefficients $A_s^m(\omega,k)$ and $C_s^m(\omega,k)$ are similar to those for the normal fracture discontinuity problem. The boundary conditions of the shear fracture discontinuity problem have been described by Guo and Gurevich (2020b). Finally, the problem reduces to solving the Fredholm integral of the second kind. The solution method is similar to that of Guo and Gurevich (2020b). The difference is that we add the influence of the microcrack-to-pore squirt flow through the constitutive Eqs. (6) and (13). For simplicity, we provide the specific solutions for the shear fracture discontinuity problem in Appendix C.

2.6. P- and SV-wave velocity and attenuation

According to Galvin and Gurevich (2009), the P-wave velocity and attenuation are controlled by the far-field scattering amplitude $f_1(\omega,\theta)$ of the fracture, which can be expressed as (Guo and Gurevich, 2020b):

$$f_1(\omega,\theta)=\frac{k_1^2}{u_0}\sum_{m=0}^{\infty}(-i)^m\cos\theta\left[A_n^m(\omega,k_1\sin\theta)+A_s^m(\omega,k_1\sin\theta)\right], \tag{38}$$

Similarly, for the SV-wave, the far-field scattering amplitude can be written as follows (Guo et al., 2022b):

$$f_3(\omega,\theta)=\frac{\rho u_\theta}{u_0e^{ik_3\rho}}=\frac{k_3^3}{u_0}\sum_{m=0}^{\infty}i(-i)^m\frac{\sin 2\theta}{2}C^m(\omega,k_3\sin\theta). \tag{39}$$

where the coefficient $C^m(\omega,k_3\sin\theta)$ is the linear superposition of the normal fracture discontinuity coefficient $C_n^m(\omega,k_3\sin\theta)$ and the shear fracture discontinuity coefficient $C_s^m(\omega,k_3\sin\theta)$.

Through the Foldy approximation (Foldy, 1945), the complex effective P- and SV-wavenumber of a microcracked porous rock containing aligned penny-shaped fractures can be written as:

$$\overline{k}_i(\omega,\theta)=k_i\left[1+\frac{4\pi n_0}{k_i^2}f_i(\omega,\theta)\right]^{1/2},\quad i=1,\ 3, \tag{40}$$

where $n_0 = \varepsilon/a^3$ represents the fracture number density, $a = d/2$ represents the radius of the fracture center plane, and ε denotes the fracture density.

When a P- or SV-wave is incident along the z-axis (Fig. 2), the complex effective P- or SV-wavenumber of randomly oriented penny-shaped fractures (isotropic distribution) can be expressed as (Zhang and Gross, 1993):

$$\bar{k}_i^{3D\_random}(\omega) = k_i\left[1 + \frac{2\pi n_0}{k_i^2}\int_0^{\pi} f_i(\omega,\theta)\sin\theta \mathrm{d}\theta\right]^{1/2}, \quad i = 1,\ 3, \tag{41}$$

Finally, the P- and SV-wave velocity and attenuation can be calculated by the complex effective wavenumbers, as follows:

$$\begin{cases} V_i(\omega) = \dfrac{\omega}{\mathrm{Re}(\bar{k}_i)} \\ Q_{\mathrm{att},i}^{-1}(\omega) = \dfrac{2\mathrm{Im}(\bar{k}_i)}{\mathrm{Re}(\bar{k}_i)} \end{cases}, \quad i = 1,\ 3. \tag{42}$$

where Re(*) and Im(*) refer taking the real and imaginary part operators, respectively.

3. Results

3.1. Modeling parameters

To investigate the influence of the microcrack squirt flow and its coupling effects with the FB-WIFF and ES of fractures, we simulated the velocity and attenuation of the plane P- and SV-wave propagating in a saturated microcracked porous sandstone containing aligned penny-shaped fractures. Unless otherwise specified, the modeling parameters that we used for the rock background, microcracks, and fractures were presented in Table 1.

3.2. Influence of wave incidence angle

Fig. 3a and 3b portray the variations in the P-wave velocity and attenuation with frequency under wave incidence angles of 0°, 30°, 45°, 60° and 90°. We also calculated the corresponding cases without fractures (WFs, shown as dashed lines). We observed that in the FB-WIFF regime, the velocity and attenuation decreases with the increase in incidence angle. Notably, the FB-WIFF attenuation mechanism at waves parallel to the fracture plane nearly vanishes but is not zero because of Poisson effect; meanwhile, the ES attenuation of fractures also disappears, and the high frequency band is controlled by the microcrack squirt flow. In the ES-controlled frequency band, the P-wave velocity first slightly decreases, for which the ratio of wavelength to fracture diameter is about π, which means that Rayleigh scattering occurs. Then, the velocity increases with frequency, and the ratio of wavelength to fracture diameter is approximately 1.13, producing stochastic/Mie scattering (Mavko et al., 2020). When the fracture thickness tends to zero, the ES attenuation mechanism disappears, and the fluid within the fracture is incompressible. The velocity and attenuation are mainly influenced by microcrack squirt flow and the FB-WIFF of fractures.

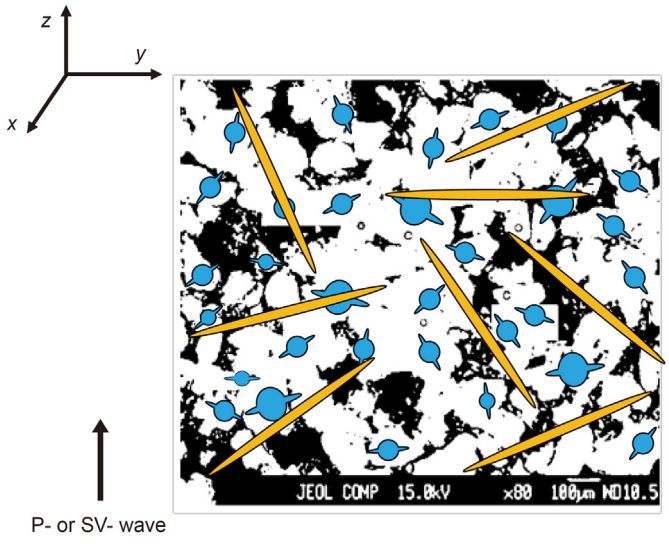

Fig. 2. Saturated isotropic microcracked porous rock matrix containing randomly oriented 3D penny-shaped fractures, and incidence of P- or SV-wave along the z-axis.

Fig. 4a and 4b portray the variations in SV-wave velocity and attenuation with frequency under incidence angles of 0°, 30°, 45°, 60° and 90°. The corresponding cases of WF are shown by dashed lines. In the FB-WIFF-controlled regime, the velocity dispersion and attenuation of the SV-wave velocity both vanish when the incident angle is 0° and 90° due to the zero effective normal stress. The maximum velocity dispersion and attenuation caused by the FB-WIFF of fractures occur when the incident angle is close to 45°. This is because the normal stress at this angle is the largest. Similar results were also reported by Guo et al. (2018b) and Song et al. (2020). In the ES effects region, the maximum attenuation occurs at an incidence angle of 0° due to the maximum shear stress. We also observed that the SV-wave velocity dispersion and attenuation caused by the ES of fractures' surface become the weakest due to the minimum shear stress at the 45° incidence angle. Similar to those of the P-wave, when the fracture thickness closes to zero at an incident angle of 45°, the SV-wave velocity dispersion and attenuation caused by the ES vanish. For the control region of microcrack squirt flow, velocity becomes minimally dependent on the incident angle because the pore–microcrack structure is randomly oriented in the background, and the slight angle dependence is from the coupling effect with the ES of the fractures.

For randomly oriented fractures, the FB-WIFF and ES attenuation caused by the fractures does not change with the P- and SV-wave incident angles. This means that the intensities of the FB-WIFF and ES are averaged owing to the random orientation of fractures, especially for the ES attenuation of SV waves. The randomly oriented fractures do not affect the microcrack squirt

Table 1
Parameters used for modeling calculations.

Symbol	Definition	Unit	Value
Porous background properties			
K_s	Bulk modulus of solid	GPa	37.9
μ_s	Shear modulus of solid	GPa	32.6
ρ_s	Solid density	kg/m^3	2650
φ	Porosity	%	8.00
κ_0	Static Darcy permeability	m^2	10^{-15}
K_f	Fluid bulk modulus	GPa	2.25
ρ_f	Fluid density	kg/m^3	1000
η	Fluid viscosity	Pa·s	10^{-3}
Microcrack properties			
ε_{mic}	Microcrack density	/	0.100
γ_{mic}	Microcrack aspect ratio	/	0.004
Fracture properties			
d	Fracture diameter	m	1.000
h	Fracture thickness	m	0.010
ε	Fracture density	/	0.050

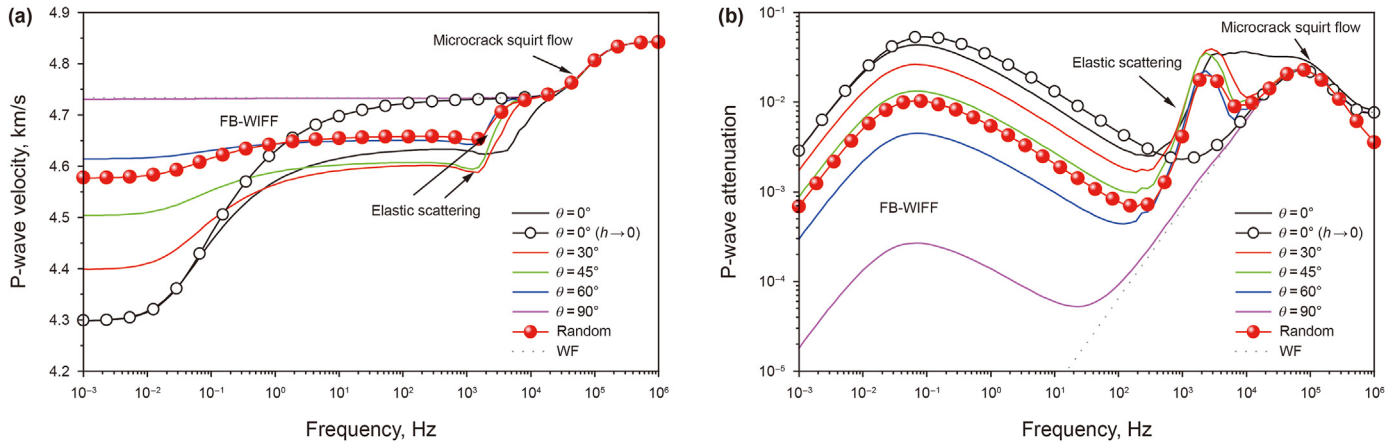

Fig. 3. Variations in P-wave velocity (a) and attenuation (b) with frequency under incidence angles of 0°, 30°, 45°, 60° and 90° in saturated microcracked porous rock with fractures. Note: WF (dashed lines) indicates results without fractures.

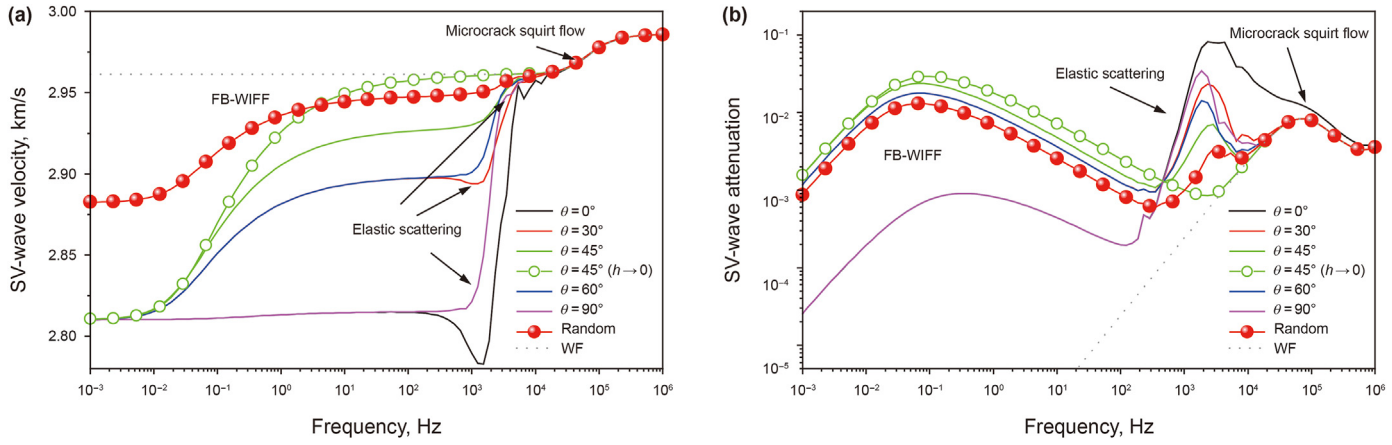

Fig. 4. Variations in SV-wave velocity (a) and attenuation (b) with frequency under incidence angles of 0°, 30°, 45°, 60° and 90° in saturated microcracked porous rock with fractures. Note: WF (dashed lines) indicates results without fractures.

flow mechanism because in the modified constitutive Eq. (6), microcracks are randomly distributed in the background medium as a part of the pore structure. Therefore, the P- and SV-wave velocities and attenuation of randomly oriented fractures and aligned fractures coincide in the high-frequency microcrack squirt flow region.

3.3. Influence of microcrack density and aspect ratio

Figs. 5 and 6 illustrate the variation in P- and SV- wave velocity dispersion and attenuation at different microcrack densities. We also calculated the wave incident normal to the fracture surface and the corresponding WF cases. In general, the P- and SV- wave velocities decrease with an increase in microcrack density. This occurs because microcracks affect the elastic properties of the rock background, and an increase in microcrack density reduces the effective stiffness of the background medium. From the perspective of wave attenuation, the increase in microcrack density not only increases the attenuation of the microcrack squirt flow but also slightly moves the characteristic frequency to a lower frequency. Compared with microcrack squirt flow, the FB-WIFF and ES attenuation mechanisms of fractures are independent of the microcrack density. When the microcrack density approaches zero, the microcrack squirt flow attenuation mechanism disappears, and the wave velocity and attenuation of the fractured rock are mainly controlled by the FB-WIFF and ES of fractures, and Biot flow mechanisms.

Figs. 7 and 8 show the variations in the P- and SV- wave velocity dispersion and attenuation at different microcrack aspect ratios ranging from 0.0001 to 0.008. The wave incidence angle is 0°, and the corresponding cases of the WF are shown as dashed lines. The microcrack squirt flow moves to a higher frequency with an increase in the microcrack aspect ratio. This is because the microcrack squirt flow characteristic frequency is proportional to the cubic aspect ratio of the microcrack (O'Connell and Budiansky, 1977; Gurevich et al., 2010). For P waves, the coupling of the microcrack squirt flow with the FB-WIFF and ES of the fractures strongly affects the velocity and attenuation. However, for SV waves, the coupling effects of the microcrack squirt flow with the ES of the fractures are negligible. This is because the attenuation of the SV wave caused by microcracks is much smaller than that caused by fractures. This means that the ES can be the main attenuation mechanism for SV waves when the wave incidence is normal to the fracture surface.

3.4. Influence of fluid viscosity and background static permeability

According to the numerical simulation results provided in Section 3.2, we found that the maximum FB-WIFF of the P- and SV-wave appears at incident angles of 0° and 45°, respectively.

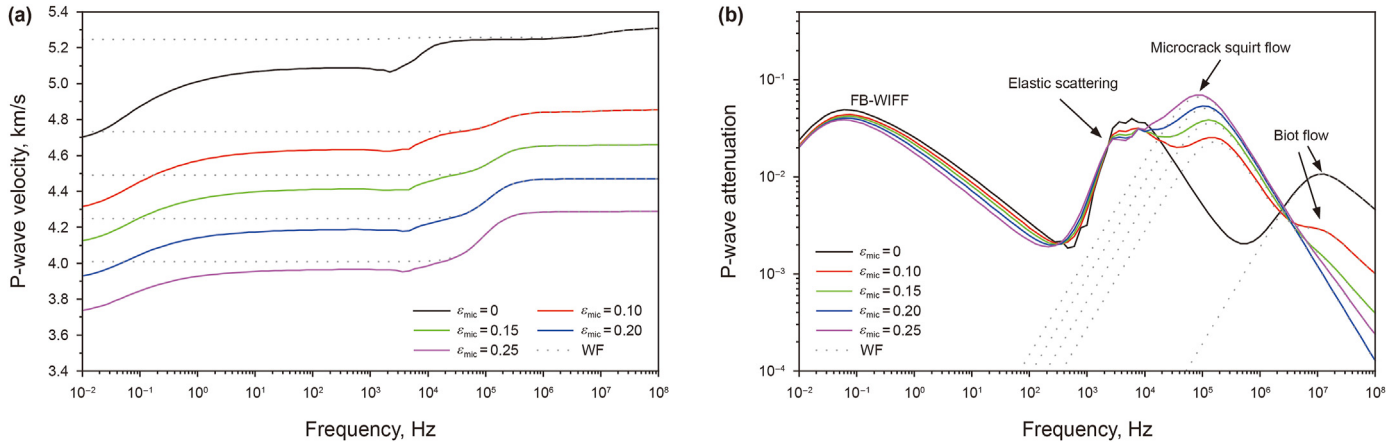

Fig. 5. Variations in P-wave velocity (a) and attenuation (b) with frequency under different microcrack densities at normal incidence in saturated microcracked porous rock with aligned fractures. Note: WF (dashed lines) indicates corresponding results without fractures.

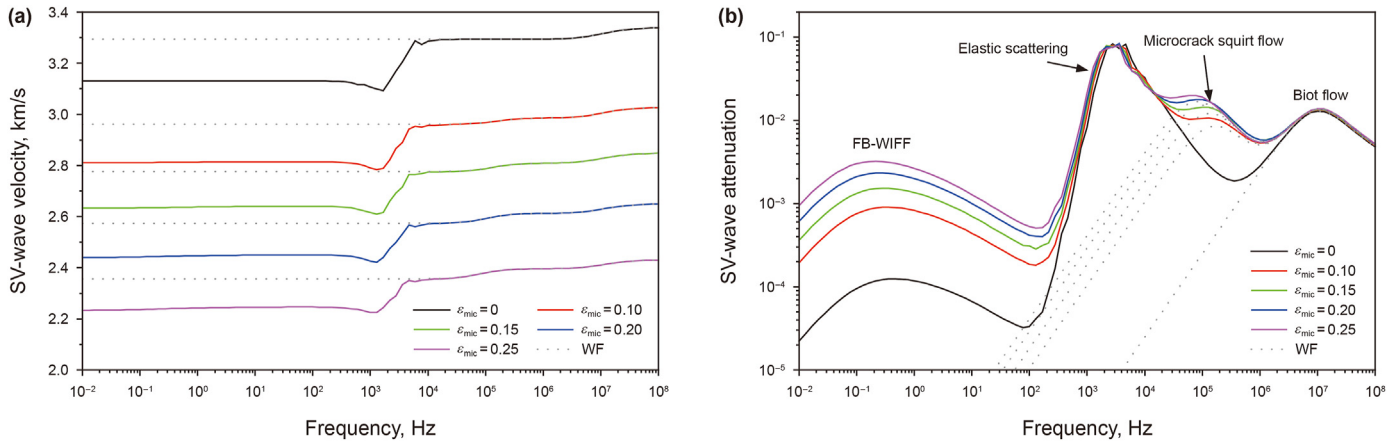

Fig. 6. Variations in SV-wave velocity (a) and attenuation (b) with frequency under different microcrack densities at normal incidence in saturated microcracked porous rock with aligned fractures. Note: WF (dashed lines) indicates corresponding results without fractures.

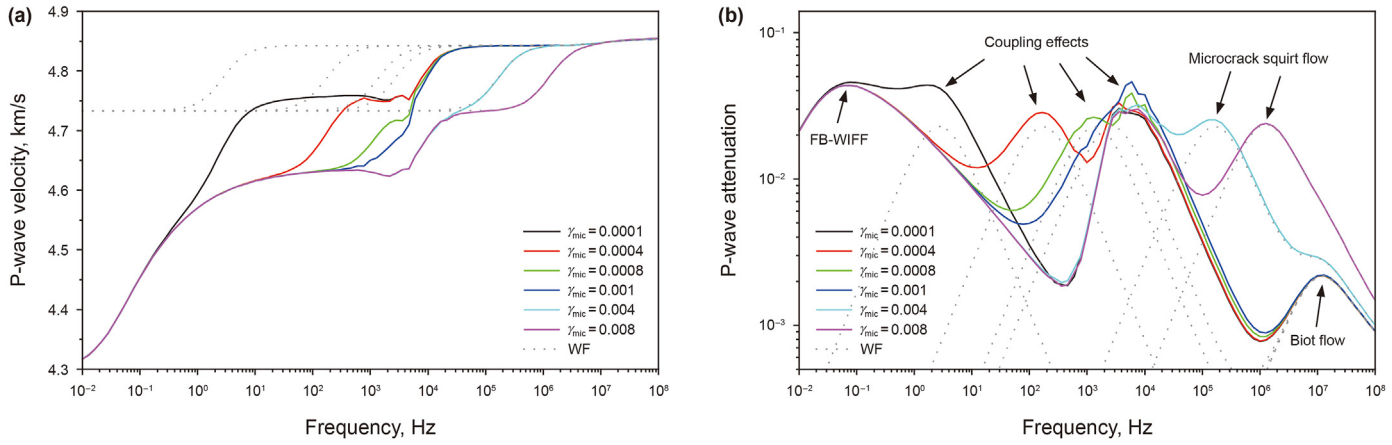

Fig. 7. Variations in P-wave velocity (a) and attenuation (b) with frequency under microcrack aspect ratios of 0.0001–0.008 at normal incidence in saturated microcracked porous rock with aligned fractures. Note: WF (dashed lines) indicates corresponding results without fractures.

Therefore, we investigated the effects of fluid viscosity and background static permeability on the velocity and attenuation of P- and SV-wave at these two angles.

Figs. 9 and 10 show the influence of fluid viscosity on the P- and SV-wave velocity and attenuation at incident angles of 0° and 45°, respectively. We also calculated the corresponding WF cases using dashed lines. The results showed that the ES attenuation mechanism of fractures is almost independent of the fluid viscosity. This is

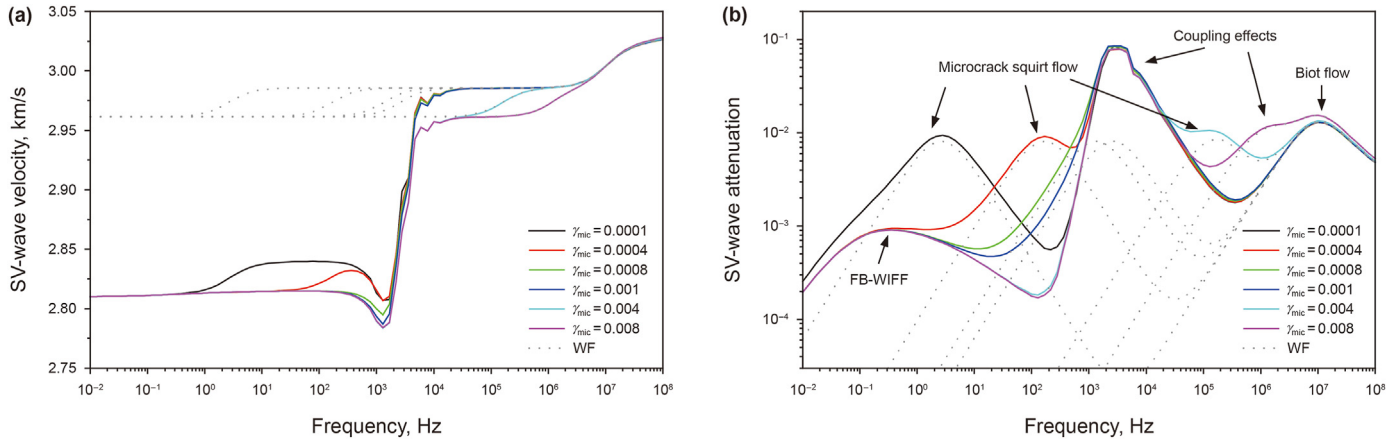

Fig. 8. Variations in SV-wave velocity (a) and attenuation (b) with frequency under microcrack aspect ratios of 0.0001–0.008 at normal incidence in saturated microcracked porous rock with aligned fractures. Note: WF (dashed lines) indicates corresponding results without fractures.

due to the ES characteristic frequency not being affect by the fluid viscosity (Guo et al., 2018c; Guo and Gurevich, 2020a). However, the increase in fluid viscosity causes the FB-WIFF of fractures, and the microcrack squirt flow shifts toward a lower frequency. This occurs because the increase in fluid viscosity increases the time required for the fluid in the fractures and microcracks to flow into the pore space. Regarding the influence of the background static permeability (Figs. 11 and 12), the FB-WIFF characteristic attenuation frequency shifts to a higher frequency with an increase in the background static permeability. However, the microcrack squirt flow is almost unaffected because the FB-WIFF characteristic frequency is controlled by both the background static permeability and fluid viscosity (Galvin and Gurevich, 2009), however, the characteristic frequency of microcrack squirt flow is independent of the background static permeability (Gurevich et al., 2010). For both P- and SV- wave, between the frequencies of 10^3 Hz and 10^4 Hz, the WF curves with a background static permeability of 10^{-12} m^2 have an inverse attenuation peak relative to the microcrack squirt flow attenuation peak. This is because the frequency shift in the Biot flow toward a lower frequency with the increase in static permeability. Compared with the P-wave attenuation, we observed that the SV-wave attenuation peak caused by the Biot flow frequency shift. This occurs because the Biot flow in P-wave is smaller than the microcrack squirt flow and has a stronger influence on the SV waves at high frequencies.

When the characteristic frequency of microcrack squirt flow occurs in the frequency range of 10^2–10^5 Hz (Figs. 9 and 10), the microcrack squirt flow and ES attenuation mechanism of the fractures are coupled. The results showed that the Rayleigh scattering phenomenon is weakened, especially for P waves. At lower frequencies, the coupling effect of the FB-WIFF and microcrack squirt flow is controlled by the relative intensity between the two attenuation mechanisms for both P and SV waves.

3.5. Influence of fluid bulk modulus

Figs. 13 and 14 show the influence of fluid bulk modulus on the P- and SV-wave velocity and attenuation at incident angles of 0° and 45°, respectively. The corresponding WF cases are shown as dashed lines. For both P and SV waves, the wave velocity increases with the increase in the fluid bulk modulus because an increase in the fluid bulk modulus decreases the compliance of the rock. The attenuation of the FB-WIFF of fractures and microcrack squirt flow decrease with a decrease in the fluid bulk modulus. This occurs because the decrease in the fluid bulk modulus results in smaller fluid pressure differences between the fractures or microcracks and the background pores. Conversely, a decrease in the fluid bulk modulus increases the ES attenuation because the fluid bulk

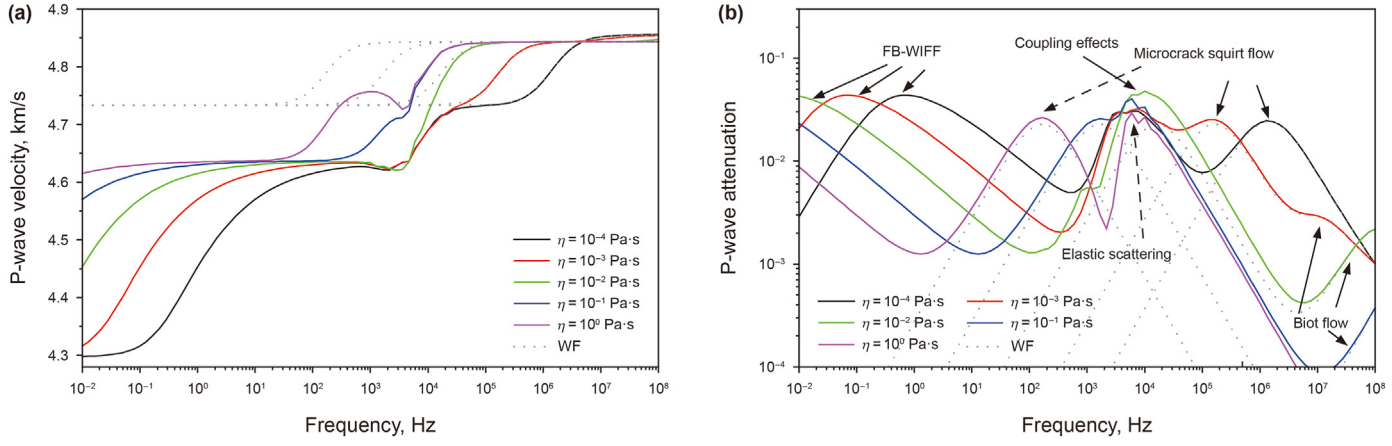

Fig. 9. Variations in P-wave velocity (a) and attenuation (b) with frequency under fluid viscosities of 10^{-4} Pa s, 10^{-3} Pa s, 10^{-2} Pa s, 10^{-1} Pa s and 10^{0} Pa s at normal incidence in saturated microcracked porous rock with aligned fractures. Note: WF (dashed lines) indicates corresponding results without fractures.

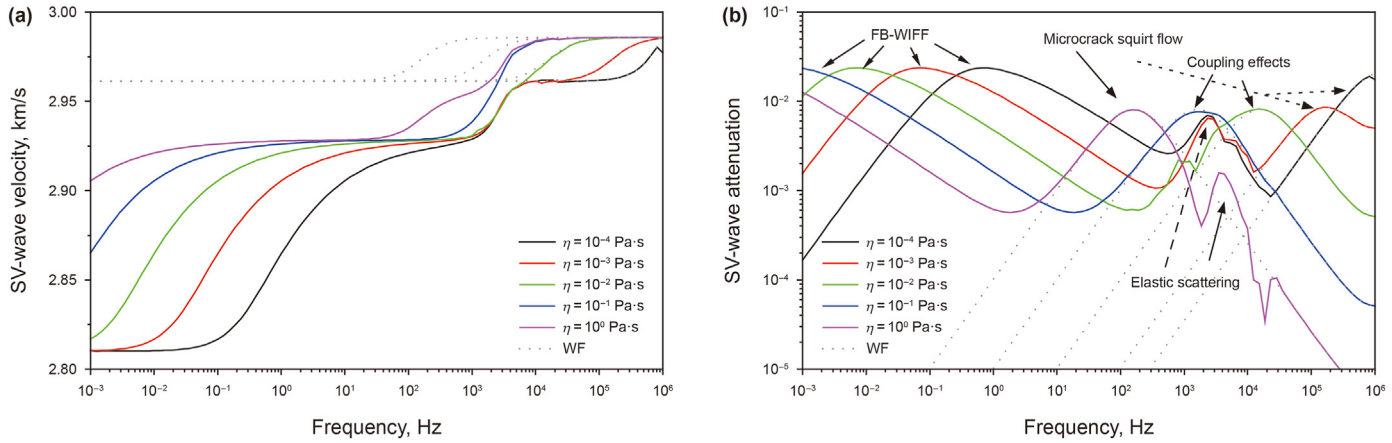

Fig. 10. Variations in SV-wave velocity (a) and attenuation (b) with frequency under fluid viscosities of 10^{-4} Pa s, 10^{-3} Pa s, 10^{-2} Pa s, 10^{-1} Pa s and 10^{0} Pa s at incident angle of 45° in saturated microcracked porous rock with aligned fractures. Note: WF (dashed lines) indicates corresponding results without fractures.

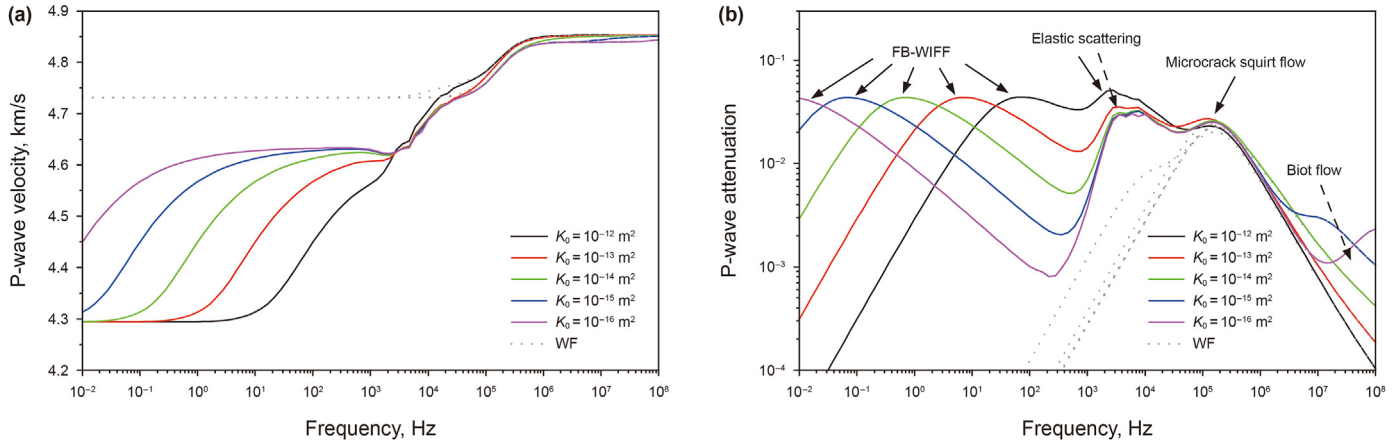

Fig. 11. Variations in P-wave velocity (a) and attenuation (b) with frequency under background static permeabilities of 10^{-12} m^2, 10^{-13} m^2, 10^{-14} m^2, 10^{-15} m^2 and 10^{-16} m^2 at normal incidence in saturated microcracked porous rock with aligned fractures. Note: WF (dashed lines) indicates corresponding results without fractures.

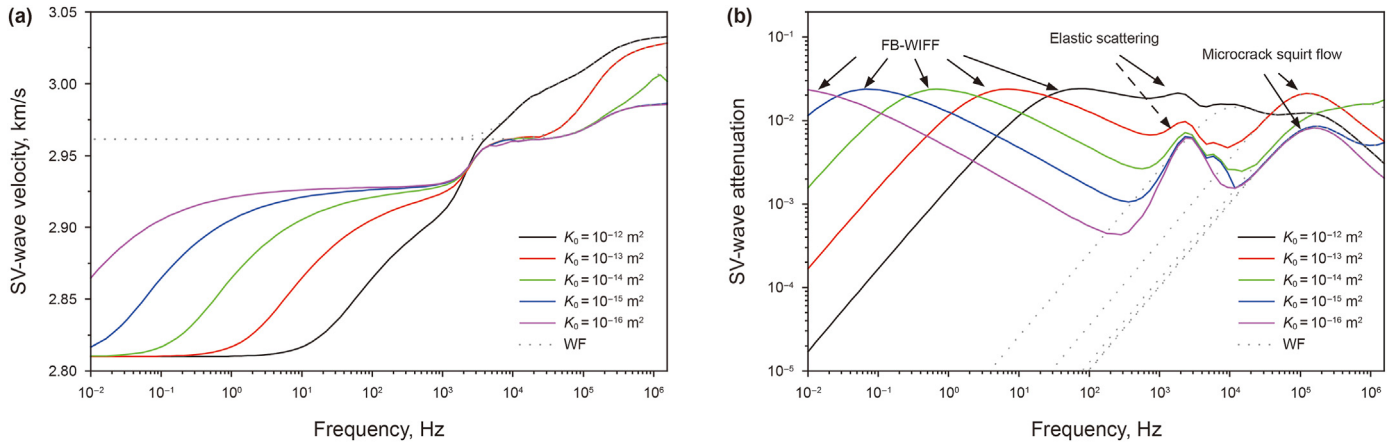

Fig. 12. Variations in SV-wave velocity (a) and attenuation (b) with frequency under background static permeabilities of 10^{-12} m^2, 10^{-13} m^2, 10^{-14} m^2, 10^{-15} m^2 and 10^{-16} m^2 at incident angle of 45° in saturated microcracked porous rock with aligned fractures. Note: WF (dashed lines) indicates corresponding results without fractures.

modulus is negatively correlated with the scattered solid and the relative fluid displacements in the fracture normal discontinuity boundary condition in Eq. (17). Similarly, the fracture thickness is positively correlated with that in Eq. (17). Therefore, the ES attenuation decreases with a decrease in the fracture thickness. For simplicity, we did not calculate the simulation results of fracture thickness in this study; meanwhile, similar results of P waves can also be found in Guo and Gurevich (2020a) and Song et al. (2021).

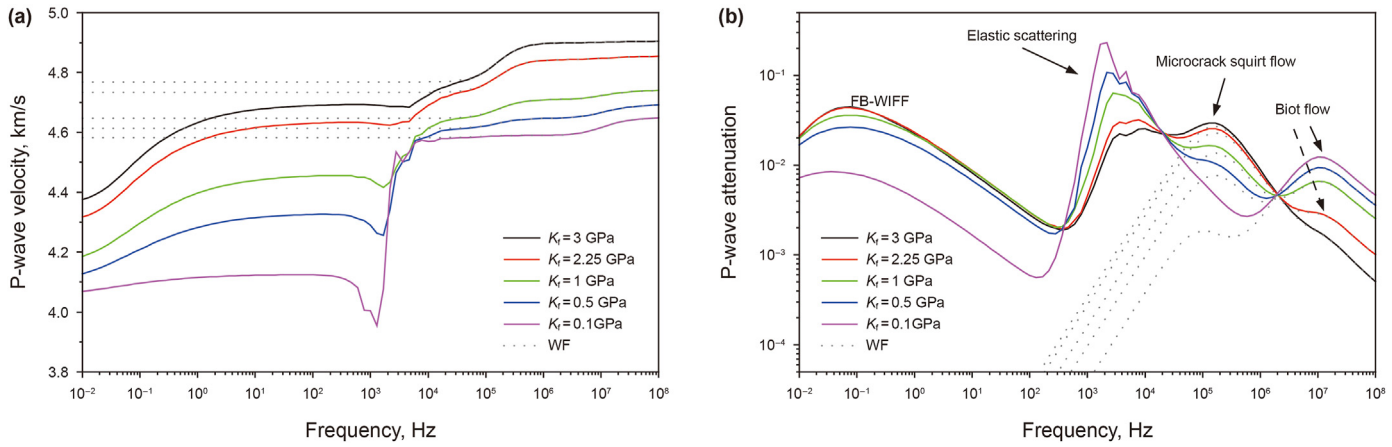

Fig. 13. Variations in P-wave velocity (a) and attenuation (b) with frequency under fluid bulk moduli of 3 GPa, 2.25 GPa, 1 GPa, 0.5 GPa and 0.1 GPa at normal incidence in saturated microcracked porous rock with aligned fractures. Note: WF (dashed lines) indicates corresponding results without fractures.

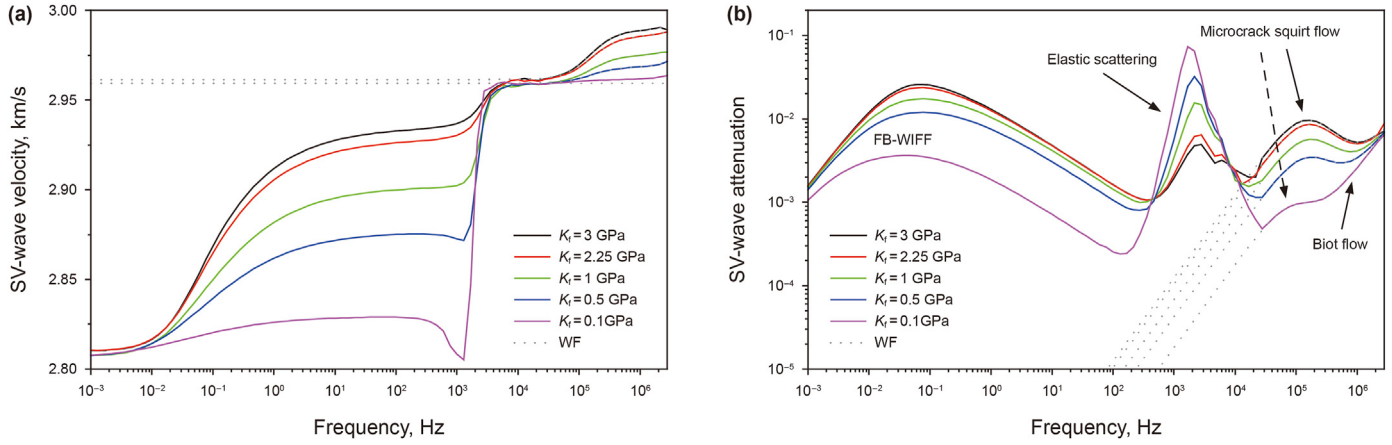

Fig. 14. Variations in SV-wave velocity (a) and attenuation (b) with frequency under fluid bulk moduli of 3 GPa, 2.25 GPa, 1 GPa, 0.5 GPa and 0.1 GPa at an incident angle of 45° in saturated microcracked porous rock with aligned fractures. Note: WF (dashed lines) indicates corresponding results without fractures.

The influence of the fracture thickness can be neglected (Song et al., 2021).

4. Comparison with existing models

In order to verify the accuracy of our model, we compared our P- and SV-wave models with that of Guo and Gurevich (2020a) (G-G model) and the interpolation approach model (I-A model, Guo et al., 2018b) at the model limit where the microcrack density close to zero. Fig. 15a and b shows the variations in the P-wave velocity and attenuation at incidence angle of 0°. We calculated the results at a fracture thickness of 0.01 m and a fracture thickness approaching zero for comparison. The results of both cases were in good agreement with those produced by the G-G model. The proposed P-wave model can be degenerated into the P-wave model proposed by Guo and Gurevich (2020a) when the microcrack density tends to zero at normal incidence.

Fig. 16a and b compares the results obtained with the proposed model for SV waves with those obtained by the I-A model at incidence angle of 45°. Similar to P waves, we calculated the SV-wave model results when the fracture thickness is 0.01 m and the thickness approaches zero. The results showed that the velocity and attenuation of SV waves caused by the FB-WIFF of fractures calculated by our model are in agreement with those calculated by the I-A model. The difference in the low-frequency range (10^{-3}~10^{-1} Hz) may be explained by the approximation in the I-A model, where the influence of SV-wave relaxation frequency changes is not considered.

5. Comparison with previous experimental data

To validate our model, we compared the theoretical P- and SV-wave predictions with the ultrasonic laboratory measurements on a synthetic-fluid-saturated rock sample permeated by aligned penny-shaped fractures reported by Tillotson et al. (2014). The samples were made of sand silica-gel and kaolinite mixture by continuous layered stacking. The aluminum discs with a certain thickness were randomly distributed on the surface of each layer. After baking at high temperature, solid silica cement is produced around the sand grains. Then, the aluminium discs are melted with acid, leaving penny-shaped cavities which represent the cracks. For the saturated sample, the porosity, density and permeability are 0.33, 2065 kg/m^3 and 21 $\times$ 10^{-15} m^2, respectively. The fluid bulk modulus, fluid viscosity and fluid density are 2.16 GPa, 10^{-3} Pa s and 1000 kg/m^3, respectively. For the fracture properties, the fracture density is 0.03, the fracture diameter and fracture thickness are 5.82 mm and 0.2497 mm, respectively. And the solid grain bulk and shear modulus are 37 GPa and 21 GPa respectively. The other

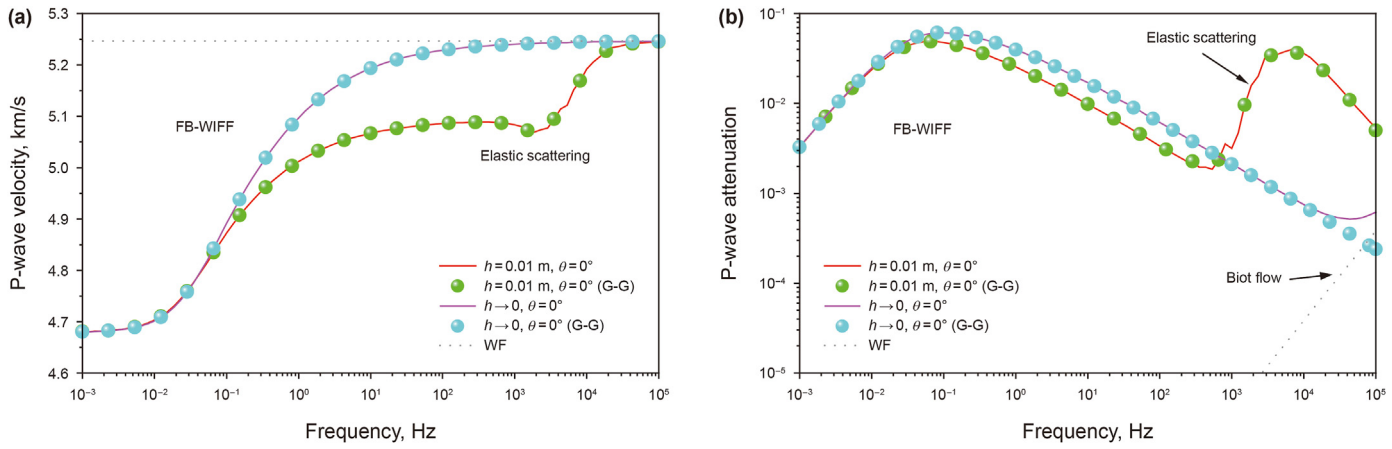

Fig. 15. Variations in P-wave velocity (a) and attenuation (b) with frequency at normal incidence. Note: We calculated the solid lines and scattered points using our model and the G-G model (Guo and Gurevich, 2020a), respectively. WF (dashed lines) indicates corresponding results without fractures.

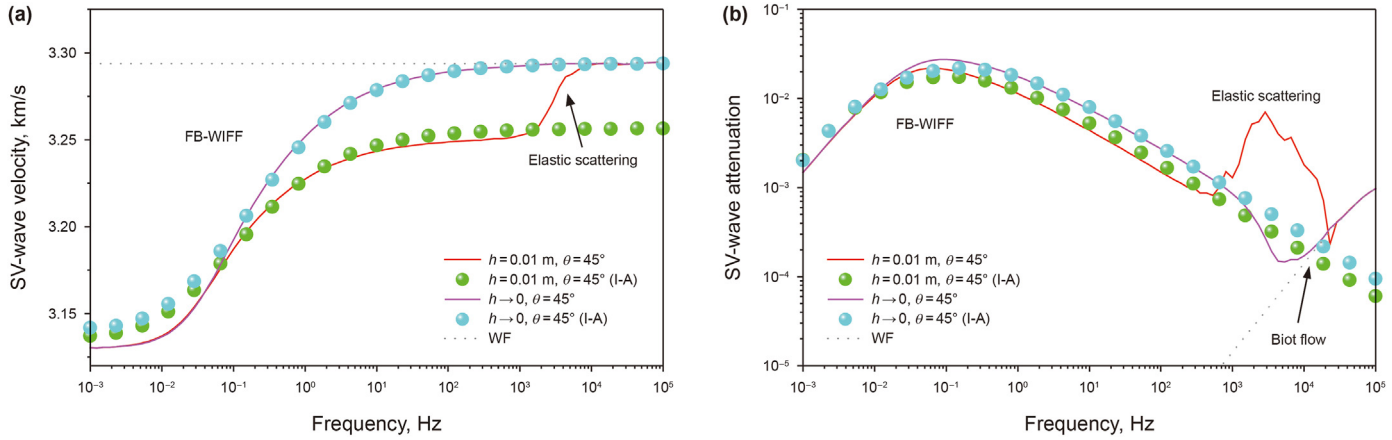

Fig. 16. Variations in SV-wave velocity (a) and attenuation (b) with frequency at incidence angle of 45°. Note: We calculated the solid lines and scattered points using our model and the I-A model (Guo et al., 2018b), respectively. WF (dashed lines) indicates corresponding results without fractures.

saturated sample parameters can also be found in Tillotson et al. (2014) and Guo and Gurevich (2020b). The central frequency for the transducers is 500 kHz. The measurement error for P- and SV-wave velocities was ±0.6%, whereas that for attenuation was approximately ±20%. A similar comparison was performed by Guo and Gurevich (2020b). However, they used this set of laboratory data to verify the oblique incidence model of P waves in a porous background medium that contained a set of aligned fractures. In their study, they subtracted the measured attenuation by the value at incidence angle of 90° to reduce the influence of attenuation mechanisms other than FB-WIFF and ES, such as squirt flow at the grain contacts. Notably, they found that the theoretical predictions were consistent with the measured results at approximately 150 kHz due to the largely attenuated wave energy at the central frequency of the transducer (500 kHz). In this study, we considered microcrack squirt flow, which we used to simulate the squirt flow between grains. We compared the original experimental data, without subtracting the parallel incidence attenuation, with the model predictions to illustrate the effectiveness of the proposed model. We set the microcrack density and aspect ratio to 0.015 and 0.0073, respectively, which are the best values for fitting the measured results.

Fig. 17 compares the P-wave laboratory data with the theoretical predictions at 150 kHz. The dashed lines represent the theoretical model predictions reported by Guo and Gurevich (2020b). The theoretical predictions of P-wave velocities agree with the laboratory data and are lower than the predictions reported by Guo and Gurevich (2020b). This is owing to the influence of microcracks. In the comparison with laboratory P-wave attenuation data, the theoretical predictions more strongly agree with the laboratory attenuation data than the predictions of Guo and Gurevich (2020b). Fig. 18 compares the SV-wave laboratory data with the theoretical predictions at 150 kHz. The dashed lines indicate the predictions of Guo et al. (2022b) for the limiting case where the fractures are parallel to each other. The solid lines represent the theoretical predictions produced by our model considering the influence of microcracks. Notably, our theoretical predictions of SV-wave velocities agree well with the laboratory data. However, the theoretical predictions of SV-wave attenuation are much lower than the laboratory data. The difference between the laboratory SV-wave attenuation data and the theoretical prediction may be owing to multishaped grain contacts. As the shapes of grain contacts in the rock differ, only considering a single microcrack aspect ratio for predicting the squirt flow attenuation may result in a large error. Similar prediction errors of the SV-wave attenuation were also shown by the model limits of Guo et al. (2022b), which are indicated by the dashed line.

The comparisons of P and SV waves with the laboratory data of

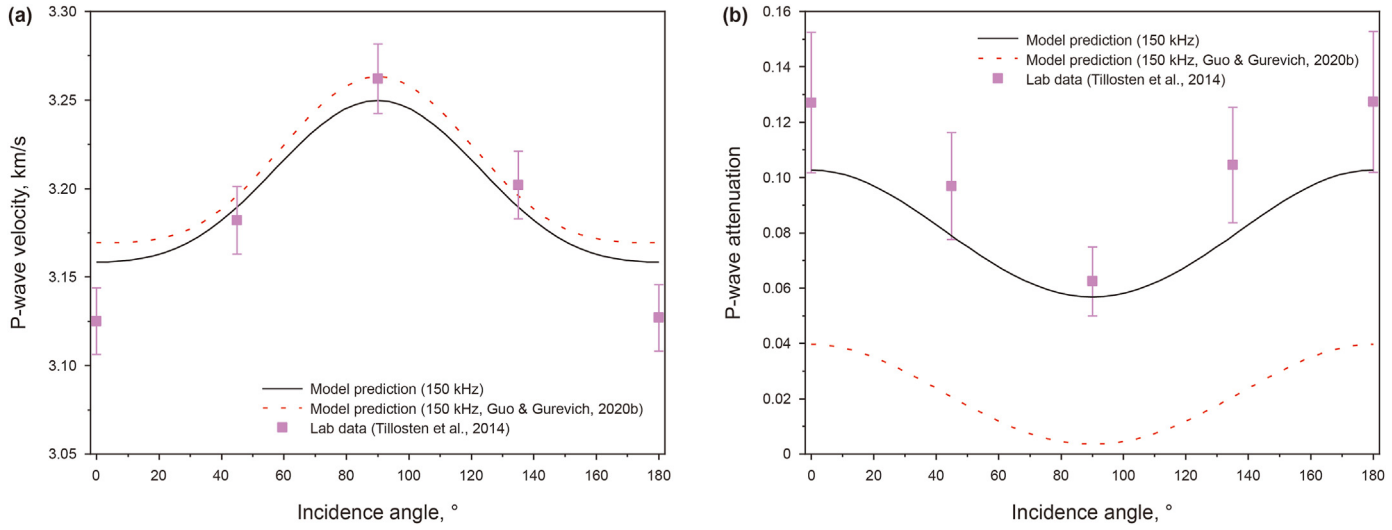

Fig. 17. Model-predicted P-wave velocity (a) and attenuation (b) versus laboratory data (Tillotson et al., 2014) for different incident angles. Red dashed lines represent model-predicted results of Guo and Gurevich (2020b). Black solid lines indicate results predicted by our model.

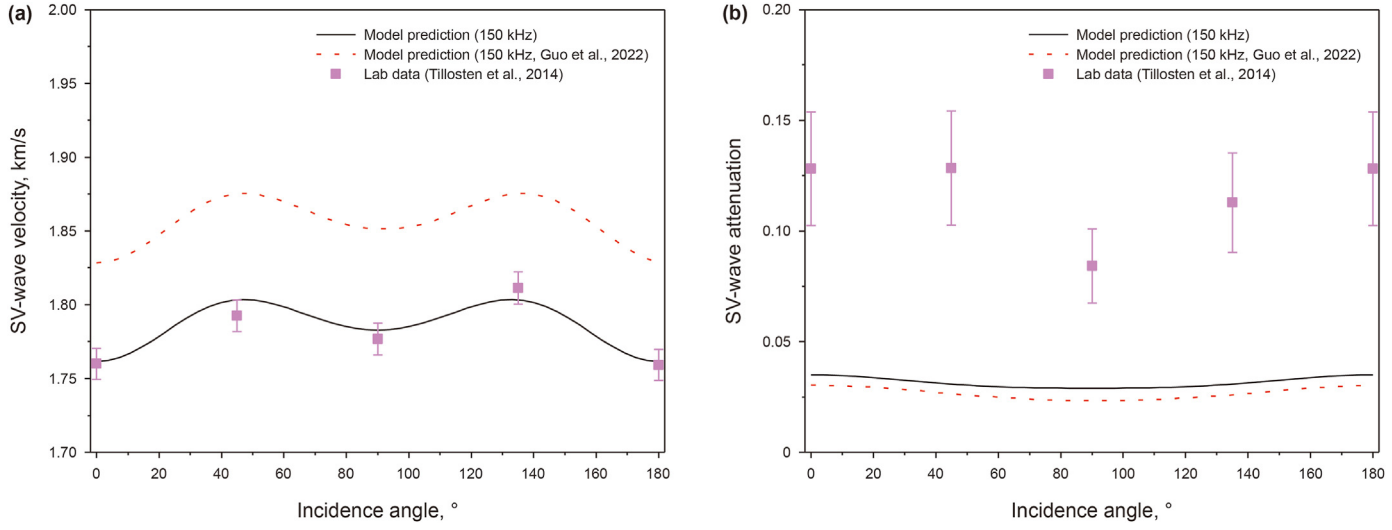

Fig. 18. Model-predicted SV-wave velocity (a) and attenuation (b) versus laboratory data (Tillotson et al., 2014) for different incident angles. Red dashed lines represent model limit prediction results of Guo et al. (2022b). Black solid lines indicate results predicted by our model.

Tillotson et al. (2014) illustrated that our model results are nearly consistent with the laboratory measurements. This indicated that, in addition to the FB-WIFF and ES, the microcrack squirt flow can also strongly contribute to the seismic dispersion and attenuation. Our model can model all these mechanisms' effects and improves the prediction accuracy of measured data.

6. Discussions

6.1. Extension to multiset fractures model with different orientations

In this study, we investigated the single-set fracture model with identically oriented and randomly oriented fractures. However, in unconventional reservoir exploration, sweet-spot areas often contain multiple sets of fractures with different orientations (Nelson, 2001). Therefore, dynamic wave models must be extended to rocks containing multioriented fracture sets. Similar to Eq. (41), following the Foldy (1945) approximation, the complex effective P- and SV-wavenumbers for multioriented fracture sets can be written as

$$\overline{k}_i^{\text{mulit-set}}(\omega) = k_i\left[1+\frac{4\pi}{k_i^2}\sum_{j=1}^{\text{Nf}} n_j f_j(\omega,\theta_j,d_j,h_j)\right]^{1/2}, \quad i=1,\ 3;\ j=1,\ 2,\ \ldots,\ \text{Nf}, \tag{43}$$

where Nf represents the total number of fracture sets in the rock; $f_j(\omega,\theta_j,d_j,h_j)$ represents the effective far-field scattering amplitude for the jth-oriented fracture set with the jth fracture diameter and fracture thickness; θ_j corresponds to the dip angle of the jth fracture set with respect to the x-y plane and the wave (P- or SV-wave) incident along the z-axis.

For actual fractured tight reservoirs, the background microcracks may also contain different microcrack densities and aspect

ratios. Under this condition, the microcrack squirting function can be extended as (Wang and Tang, 2021)

$$S^{\text{mulit-set}}(\omega) = \sum_{j=1}^{\text{Nm}} S_j(\omega), \quad j = 1,\ 2,\ \ldots,\ \text{Nm}. \tag{44}$$

where Nm is the total number of microcracks in the rock; $S_j(\omega)$ denotes the squirting function of the jth microcrack set, and its expression is the same as that in Eq. (7).

6.2. Advantages and application of our model

A critical assumption of our model is the cymbal-shaped pore-microcrack structure in the rock background (Fig. 1a). Such structures result in the squirt flow between the pores and microcracks. Hence, to apply our model in the fractured reservoir characterizations, it is essential to compare the pore-microcrack structure assumed in our model with that in the real rocks. In Fig. 19, we provide the thin section of a fractured sandstone from the Bozhong area of China. It can be found that the pore-microcrack structure observed in the thin section is approximately cymbal-shaped, which is consistent with the assumption of our model. In addition to this thin section, other studies also found a similar pore-microcrack structure (Liu et al., 2017b). Therefore, the cymbal-shaped pore-microcrack structure assumed in our model is reasonable.

In the previous models, only one or two attenuation mechanisms were considered. In contrary, our model considers multiple attenuation mechanisms at different scales, which includes the squirt flow at the microscopic scale, the WIFF at the mesoscopic scale, and the Biot's global flow and elastic scattering at the macroscopic scale. Hence, our model connects the data measured at different frequencies from the laboratory measurements (~MHz) to the sonic logging (~KHz) and seismic exploration (~Hz). This facilitates the integration of different measurement data for the exploration of the fractured reservoirs. In addition, in the cases where the characteristic frequencies of different mechanisms are close, the coupling effects between different mechanisms may give rise to a complicated attenuation behavior for the propagating waves. Under this condition, our model provides more accurate descriptions of the wave attenuation and thus is more suitable to be applied in such reservoirs.

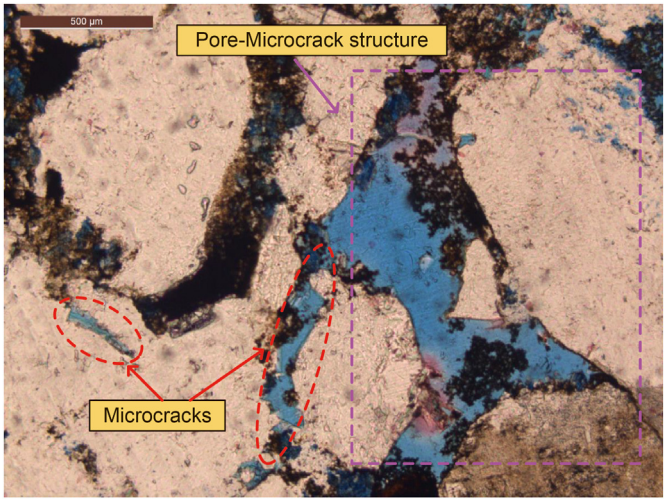

Fig. 19. Micrograph of orthogonally polarized feldspathic quartz sandstone, the observation scale is 500 μm. The microcracks indicate unfilled microcracks, and the pore-microcrack structure indicates the combination of equant spherical pores and microcracks.

To observe the multiple attenuation mechanisms and apply our model in the real fractured reservoirs, several steps can be taken. First, we can take several core samples from different areas of the reservoir, for which only the microcracks exist. We can perform the ultrasonic and low-frequency measurements on the samples to observe the wave dispersion and attenuation. Combined with other measurements, we can use the measured velocities and attenuation to invert the microcrack properties through our model. These inverted microcrack properties can be compared to other predictions or observations (such as nano-CT scans) to validate their accuracies. By using the averaged microcrack properties of these core samples as those properties for the reservoir, we can further estimate the fracture properties by our model. This can be done by using the wave velocities, attenuation, and frequency-dependent anisotropy obtained from the seismic exploration and sonic logging. Similarly, to validate the estimated fracture properties, we can compare the results with other measurements, such as resistivity imaging logging. The detailed procedure for using our model to invert the properties of the microcracks and fractures will be studied in details in the near future.

7. Conclusions

In this study, we proposed a unified model to investigate P- and SV-wave propagation and attenuation in a saturated fractured rock with a microcracked porous background medium. We considered multiple attenuation mechanisms, including the microscopic squirt flow, the mesoscopic FB-WIFF, and the macroscopic Biot's global flow and ES. We constructed theoretical models of aligned and randomly oriented fractures. The numerical results indicate that the microcrack squirt flow in the fractured rock background substantially affects the P and SV waves. The coupling effects of the microcrack squirt flow with the FB-WIFF and ES of the fractures were considerable for the P and SV waves. The maximum FB-WIFF of the P and SV waves occurs at incident angles of 0° and 45°, respectively. The influence of rock background static permeability on the attenuation of the P waves caused by ES and microcrack squirt flow can be neglected, but it more strongly influences the SV waves. Compared with aligned fracture cases, the FB-WIFF and ES attenuation intensities of the P and SV waves of randomly oriented fractures are notably averaged, especially the attenuation of the SV-wave induced by the ES.

Open research

All the theoretical results are calculated using Matlab. The codes can be obtained by contacting the authors with reasonable requests. The experimental data were provided by Tillotson et al. (2014), details of this reference can be found in the reference list.

Declaration of interests

The authors declare that they have no known competing financial interests or personal relationships that could have appeared to influence the work reported in this paper.

Acknowledgments

This work was supported by the Laoshan National Laboratory Science and Technology Innovation Project (No. LSKJ202203407), the National Natural Science Foundation of China (Grant Nos. 42174145, 41821002, 42274146), Guangdong Provincial Key Laboratory of Geophysical High-resolution Imaging Technology (2022B1212010002), and Shenzhen Stable Support Plan Program for Higher Education Institutions (20220815110144003).

Appendix A. The detailed calculation procedure of the Biot-Consistent theory

For pore-microcrack coexisting rock, the total pores can be divided into two parts of equant spherical pores and microcracks. To describe the elastic properties of this medium, O'Connell and Budiansky (1974) (OB theory) used the Self-Consistent approximation (Hill, 1965; Wu, 1966) to calculate the elastic properties of porous rocks with randomly distributed microcracks. On this basis, Thomsen (1985) proposed the Biot-Consistent theory to make the OB theory compatible with the Biot theory.

For any specific microcrack density ε_{mic} and microcrack aspect ratio γ_{mic}, the porosity of penny-shaped microcracks is expressed as follows:

$$\varphi_{mic} = \frac{4\pi\varepsilon_{mic}\gamma_{mic}}{3}. \tag{A1}$$

Assuming that Poisson's ratio satisfies the Biot-Consistent conditions of dry microcracked porous background is ν_B^*, to find ν_B^*, we set the initial value of ν_B^* as ν_1^* ($0< \nu_1^* <0.5$). Then, the dry microcracked porous background shear and bulk modulus can be written as follows:

$$\mu_d^* = \mu_s\left(1 - \frac{\varphi_p}{1-b_B} - B_B\varepsilon_{mic}\right), \tag{A2}$$

$$K_d^* = \frac{2\mu_d^*(1+\nu_1^*)}{3(1-2\nu_1^*)}, \tag{A3}$$

where

$$b_B = \frac{2(4-5\nu_1^*)}{15(1-\nu_1^*)}, \tag{A4}$$

$$B_B = \frac{32(1-\nu_1^*)(5-\nu_1^*)}{45(2-\nu_1^*)}, \tag{A5}$$

where φ_p represents the porosity of the equant spherical pores; and the total porosity $\varphi = \varphi_p + \varphi_{mic}$.

Then, the fluid pressure increment of Biot theory can be expressed as (Thomsen, 1985):

$$\frac{p_f}{\tilde{p}_f} = \frac{\alpha_B K_f}{K_d^*\left(\varphi + \frac{K_f}{K_d^*}(\alpha_B - \varphi + \varphi\alpha_B)\right)}, \tag{A6}$$

where the Biot coefficient α_B is expressed as:

$$\alpha_B = 1 - K_d^*/K_s, \tag{A7}$$

Now, the saturated bulk modulus of microcracked porous rock background is obtained as (Budiansky and O'Connell, 1980):

$$\tilde{K} = K_s\left[1 + \varphi\left(K_s/K_f - 1\right)\cdot p_f/\tilde{p}_f\right]^{-1}, \tag{A8}$$

Through the low frequency Biot-Guassmann theory (Gassmann, 1951), the classic saturated bulk modulus of Biot medium can be expressed as:

$$K_B = K_d^*\left(1 - \alpha_B\frac{p_f}{\tilde{p}_f}\right)^{-1}, \tag{A9}$$

Because the dry and saturated shear modulus of microcracked porous background are equal at low frequencies, combined Eq. (A9) with Eq. (A2), the Poisson's rate of saturated microcracked porous background can be written as:

$$\nu_{new} = \frac{1 - 2\mu_d^*/3K_B}{2 + 2\mu_d^*/3K_B}, \tag{A10}$$

The saturated bulk modulus of microcracked porous background can be yields (Budiansky and O'Connell, 1980):

$$\tilde{K}_B = K_s\left[1 - \left(1 - \frac{K_f}{K_s}\right)\left(\frac{\varphi_p}{1-a_B} + A_B\varepsilon_{mic}\right)\right]\cdot\left[1 + \frac{K_f}{K_B}\left(\frac{a_B}{1-a_B}\frac{\varphi_p}{\varphi} + \frac{A_B\varepsilon_{mic}}{\varphi}\right)\right]^{-1}, \tag{A11}$$

where

$$a_B = \frac{1+\nu_{new}}{3(1-\nu_{new})}, \tag{A12}$$

$$A_B = \frac{16(1-\nu_{new}^2)}{9(1-2\nu_{new})}. \tag{A13}$$

Repeat the above steps to compare the bulk modulus calculated in Eqs. (A8) and (A11). When the two moduli are consistent with a certain accuracy, the Biot-Consistent condition is met, and the Poisson's ratio ν_B^* of dry microcracked porous background is output.

Finally, the shear modulus of the microcracked porous rock background $\mu_0 = \mu_0(\varepsilon_{mic}, \varphi)$ in the absence of squirt flow (low frequency) can be calculated by Eq. (A2) with Poisson's rate ν_B^*. The dry bulk modulus $K_d = K_d(\varepsilon_{mic}, \varphi)$ is obtained from Eq. (A3).

Hence, the saturated bulk modulus $K_0 = K_0(\varepsilon_{mic}, \varphi)$ and the Poisson's rate $\nu_0 = \nu_0(\varepsilon_{mic}, \varphi)$ can be expressed as:

$$K_0 = K_0(\varepsilon_{mic}, \varphi) = K_d + \left(1 - \frac{K_d}{K_s}\right)^2\left[\frac{1 - K_d/K_s - \varphi}{K_s} + \frac{\varphi}{K_f}\right]^{-1}, \tag{A14}$$

$$\nu_0 = \nu_0(\varepsilon_{mic}, \varphi) = \frac{3K_0 - 2\mu_0}{2(3K_0 + \mu_0)}. \tag{A15}$$

Appendix B. General solutions of scattered wavefields from single fracture in saturated microcracked porous medium

Based on the wave propagation theory of microcracked porous

media (Tang et al., 2012), the general solutions of scattered wavefields can be obtained using Hankel transformation. Following Song's (2017) derivation, the general scattered wavefield solutions of fractured porous elastic equations can be expressed as follows:

$$u_r^m \pm u_\varphi^m = \mp \int_0^\infty \left[A^m(\omega,k)\mathrm{e}^{-Q_1 z} + B^m(\omega,k)\mathrm{e}^{-Q_2 z}\right]k^2 J_{m\pm1}(kr)\mathrm{d}k \pm \int_0^\infty C^m(\omega,k)\mathrm{e}^{-Q_3 z}Q_3 k^2 J_{m\pm1}(kr)\mathrm{d}k, \tag{B1}$$

$$u_z^m = -\int_0^\infty \left[A^m(\omega,k)Q_1\mathrm{e}^{-Q_1 z} + B^m(\omega,k)Q_2\mathrm{e}^{-Q_2 z} - C^m(\omega,k)k^2\mathrm{e}^{-Q_3 z}\right]kJ_m(kr)\mathrm{d}k, \tag{B2}$$

$$w_z^m = -\int_0^\infty \left[\begin{array}{l}\chi_1 A^m(\omega,k)Q_1\mathrm{e}^{-Q_1 z} + \chi_2 B^m(\omega,k)Q_2\mathrm{e}^{-Q_2 z} \\ -\chi_3 C^m(\omega,k)k^2\mathrm{e}^{-Q_3 z}\end{array}\right]kJ_m(kr)\mathrm{d}k, \tag{B3}$$

$$\sigma_{zr}^m \pm \sigma_{z\varphi}^m = \pm 2\mu \int_0^\infty \left[A^m(\omega,k)\mathrm{e}^{-Q_1 z}Q_1 + B^m(\omega,k)\mathrm{e}^{-Q_2 z}Q_2\right]k^2 J_{m\pm1}(kr)\mathrm{d}k \mp \mu \int_0^\infty C^m(\omega,k)\mathrm{e}^{-Q_3 z}\left(2k^2 - k_3^2\right)k^2 J_{m\pm1}(kr)\mathrm{d}k, \tag{B4}$$

$$\begin{aligned}\sigma_{zz}^m = &\int_0^\infty \left[2\mu k^2 - (\widehat{H} + \widehat{C}\chi_1)k_1^2\right]A^m(\omega,k)\mathrm{e}^{-Q_1 z}kJ_m(kr)\mathrm{d}k + \int_0^\infty \left[2\mu k^2 - (\widehat{H} + \widehat{C}\chi_2)k_2^2\right]B^m(\omega,k)\mathrm{e}^{-Q_2 z}kJ_m(kr)\mathrm{d}k \\ &- \int_0^\infty 2\mu k^2 Q_3 C^m(\omega,k)\mathrm{e}^{-Q_3 z}kJ_m(kr)\mathrm{d}k,\end{aligned} \tag{B5}$$

$$p_\mathrm{f}^m = \int_0^\infty \left[k_1^2(\widehat{C} + \widehat{M}\chi_1)A^m(\omega,k)\mathrm{e}^{-Q_1 z} + k_2^2(\widehat{C} + \widehat{M}\chi_2)B^m(\omega,k)\mathrm{e}^{-Q_2 z}\right]kJ_m(kr)\mathrm{d}k. \tag{B6}$$

where the superscript m represents the mth component; $J_m(*)$ refers to the first class of m-order Bessel functions; A^m, B^m, and C^m are the undetermined coefficients; $k_i (i = 1,2,3)$, respectively, are the complex fast P, slow P, and S wavenumbers in a saturated fractured porous rock, which can be calculated using the Biot theory formulas (Tang and Cheng, 2004; Tang et al., 2012); and parameters χ_i $(i = 1,2,3)$ are given as follows:

$$\chi_{1,2} = -\frac{\widehat{H}s_{1,2}^2 - \rho}{\widehat{C}s_{1,2}^2 - \rho_\mathrm{f}}, \tag{B7}$$

$$\chi_3 = -\rho_\mathrm{f}\big/\rho', \tag{B8}$$

where s_i $(i = 1,2,3)$ represent the fast P, slow P, and S waves, respectively, which can be calculated as follows:

$$s_i = k_i/\omega \ \ (i = 1,\ 2,\ 3). \tag{B9}$$

To satisfy the radiation condition, the uniformizing parameters Q_i $(i = 1,3)$ are expressed as:

$$Q_i = \begin{cases} -i\sqrt{k_i^2 - k^2}\,[\mathrm{Re}(k_i) > k] \\ \sqrt{k^2 - k_i^2}\,[\mathrm{Re}(k_i) < k]\end{cases}, \tag{B10}$$

and Q_2 has the following form:

$$Q_2 = -i\sqrt{k_2^2 - k^2}. \tag{B11}$$

Appendix C. Fredholm integral satisfied by shear fracture discontinuity problem

Similar to solving the normal fracture discontinuity problem in Section 2.5.1, the first step involves deducing the characteristic relationships between the scattered wavefield coefficients. Substituting the general solution of Eqs. (B5) and (B6) into the boundary conditions in Eq. (19) yields:

$$C_\mathrm{s}^m(\omega,k) = \left\{\begin{array}{l} 1 - \dfrac{k_1^2(\widehat{C} + \widehat{M}\chi_1)}{k_2^2(\widehat{C} + \widehat{M}\chi_2)} - \dfrac{k_1^2(\widehat{H} + \widehat{C}\chi_1)}{2\mu k^2} \\ + \dfrac{k_1^2(\widehat{H} + \widehat{C}\chi_1)(\widehat{C} + \widehat{M}\chi_1)}{2\mu k^2(\widehat{C} + \widehat{M}\chi_2)}\end{array}\right\}\frac{A_\mathrm{s}^m(\omega,k)}{Q_3}, \tag{C1}$$

$$B_s^m(\omega,k) = -\frac{k_1^2(\widehat{C}+\widehat{M}\chi_1)A_s^m(\omega,k)}{k_2^2(\widehat{C}+\widehat{M}\chi_2)}, \tag{C2}$$

where the subscript "s" represents the shear-fracture discontinuity problem. Substitute the general solution of Eqs. (B1) and (B4) into the boundary conditions in Eqs. (20) and (19), respectively. Then, perform some mathematical transformations, and the dual integrals for the shear fracture discontinuity can be expressed as follows:

$$\begin{cases} \int_0^\infty U_s(\omega,k)J_m(kr)\mathrm{d}k = 0, & d/2 < r < \infty \\ \int_0^\infty [1+H_s(\omega,k)]U_s(\omega,k)J_m(kr)k\mathrm{d}k = -f_s(\omega,r), & 0 \le r \le d/2 \end{cases}, \tag{C3}$$

where

$$U_s(\omega,k) = k^{-1}E_s(\omega)A_n^m(\omega,k), \tag{C4}$$

$$H_s(\omega,k) = E_s^{-1}(\omega)k^{-1}\left[L_1(\omega,k) - F_{s,2}(\omega,k)\right] - 1, \tag{C5}$$

with:

$$F_{s,2}(\omega,k) = \frac{k_1^2(\widehat{C}+\widehat{M}\chi_1)}{k_2^2(\widehat{C}+\widehat{M}\chi_2)}L_2, \tag{C6}$$

$$L_i(\omega,k) = 2Q_i - \frac{2k^2-k_3^2}{Q_3} + \frac{k_i^2\left(2k^2-k_3^2\right)(\widehat{H}+\widehat{C}\chi_i)}{2\mu k^2 Q_3}, \quad i=1,\ 2, \tag{C7}$$

where $f_s(\omega,r)$ can be obtained using Eq. (14) into the constitutive Eqs. (6) and (13), respectively.

Using the decomposition formula $e^{ik_ix} = \sum_{m=0}^{\infty}\upsilon_m i^m J_m(k_i r)\cos\varphi$, $(i=1,\ 3)$ and relationship $\mathbf{w} = \chi_i\mathbf{u}_s$, $(i=1,\ 3)$, the function $f_s(\omega,r)$ in Eq. (C3) for P and SV waves, respectively, can be written as follows:

$$f_s^{\mathrm{p}}(\omega,r) = -\upsilon_m i^m 2u_0\cos\theta J_m(k_1 r\sin\theta), \tag{C8}$$

$$f_s^{\mathrm{sv}}(\omega,r) = -\upsilon_m i^m u_0\frac{\cos 2\theta}{\sin\theta}J_m(k_3 r\sin\theta), \tag{C9}$$

where the superscripts P and SV denote the incidence of P- and SV-wave, respectively; and $E_s(\omega)$ can be expressed as:

$$E_s(\omega) = \left[\widehat{C}^2 - (\widehat{H}-\mu)\widehat{M}\right](\chi_1-\chi_2)k_1^2\Big/[\mu(\widehat{C}+\widehat{M}\chi_2)]. \tag{C10}$$

Subsequently, convert Eq. (C3) to the Fredholm integral of the second kind, as follows:

$$\Phi_s(\omega,\tau) + \int_0^{d/2} W_s(\omega,\tau,\tilde{\tau})\cdot\Phi_s(\omega,\tilde{\tau})\mathrm{d}\tilde{\tau} = F_s(\omega,\tau), \quad 0 \le \tau \le d/2, \tag{C11}$$

where

$$W_s(\omega,\tau,\tilde{\tau}) = \sqrt{\tau\cdot\tilde{\tau}}\int_0^\infty H_s(\omega,k)J_{0.5+m}(k\tau)J_{0.5+m}(k\tilde{\tau})k\mathrm{d}k, \tag{C12}$$

$$F_s(\omega,\tau) = -\frac{1}{\tau^m}\int_0^\tau \frac{f_s(\omega,r)r^{m+1}}{\sqrt{\tau^2-r^2}}\mathrm{d}r, \tag{C13}$$

and

$$U_s(\omega,k) = \sqrt{\frac{2k}{\pi}}\int_0^{d/2}\sqrt{\tilde{\tau}}\Phi_s(\omega,\tilde{\tau})J_{0.5+m}(k\tilde{\tau})\mathrm{d}\tilde{\tau}. \tag{C14}$$

Finally, the coefficients can be derived numerically in the same way as for the case of the normal fracture discontinuity.

Appendix D. Numerical solution of the Fredholm integral equation of the second kind

For both normal and shear fracture discontinuity problems, the method followed by Guo and Gurevich (2020b) is used to numerically solve the coefficients (Sherief and El-Maghraby, 2003). As mentioned in Section 2.5.1 and Appendix C, the key to solving the coefficients is to solve $\Phi_{\mathrm{n,s}}(\omega,\tilde{\tau})$ in the Fredholm integrals of the second kind. First, we rewrite the integral equations as follows:

$$\Phi_{\mathrm{n,s}}(\omega,\tau) + \int_0^{d/2} W_{\mathrm{n,s}}(\omega,\tau,\tilde{\tau})\cdot\Phi_{\mathrm{n,s}}(\omega,\tilde{\tau})\mathrm{d}\tilde{\tau} = F_{\mathrm{n,s}}(\omega,\tau), \quad 0 \le \tau \le d/2, \tag{D1}$$

where

$$W_{\mathrm{n,s}}(\omega,\tau,\tilde{\tau}) = \sqrt{\tau\cdot\tilde{\tau}}\int_0^\infty H_{\mathrm{n,s}}(\omega,k)J_{0.5+m}(k\tau)J_{0.5+m}(k\tilde{\tau})k\mathrm{d}k, \tag{D2}$$

$$F_{\mathrm{n,s}}(\omega,\tau) = -\frac{1}{\tau^m}\int_0^\tau \frac{f_{\mathrm{n,s}}(\omega,r)r^{m+1}}{\sqrt{\tau^2-r^2}}\mathrm{d}r, \tag{D3}$$

$$U_{\mathrm{n,s}}(\omega,k) = \sqrt{\frac{2k}{\pi}}\int_0^{d/2}\sqrt{\tilde{\tau}}\Phi_{\mathrm{n,s}}(\omega,\tilde{\tau})J_{0.5+m}(k\tilde{\tau})\mathrm{d}\tilde{\tau}, \tag{D4}$$

where the subscripts "n" and "s" represent the corresponding functions for normal and shear fracture discontinuity problems, respectively. Discretize Eq. (D1) within the fracture radius range (0, $d/2$); assuming that the number of discrete points is N, then, Eq. (D1) can be expressed as:

$$\left\{\sum_{j=1}^{N}\left[W_{\mathrm{n,s}}\left(\omega,\frac{d\cdot i}{2N},\frac{d\cdot j}{2N}\right)\cdot\frac{d}{2N}+\delta_{ij}\right]\right\}\cdot\Phi_{\mathrm{n,s}}\left(\omega,\frac{d\cdot j}{2N}\right) = F_{\mathrm{n,s}}\left(\omega,\frac{d\cdot i}{2N}\right) \quad i=1,\ 2,\ \ldots,\ N. \tag{D5}$$

The linear solution is $\Phi_{\mathrm{n,s}}\left(\omega,\frac{d\cdot j}{2N}\right)$; substituting it into Eq. (D4) and drive the numerical solution of $U_{\mathrm{n,s}}(\omega,k)$. Subsequently, compared with Eqs. (31) and (C4), the coefficients $A_{\mathrm{n}}^m(\omega,k)$ and $A_{\mathrm{s}}^m(\omega,k)$ can be obtained.

References

Adelinet, M., Fortin, J., Guéguen, Y., 2011. Dispersion of elastic moduli in a porous-cracked rock: theoretical predictions for squirt-flow. Tectonophysics 503 (1–2), 173–181. https://doi.org/10.1016/j.tecto.2010.10.012.

Baird, A.F., Kendall, J.M., Angus, D.A., 2013. Frequency-dependent seismic anisotropy due to fractures: fluid flow versus scattering. Geophysics 78 (2), WA111–WA122. https://doi.org/10.1190/geo2012-0288.1.

Berryman, J.G., 2006. Effective medium theories for multicomponent poroelastic composites. J. Eng. Mech. 132 (5), 519–531. https://doi.org/10.1061/(ASCE)0733-9399(2006)132:5(519).

Berryman, J.G., Wang, H.F., 1995. The elastic coefficients of double-porosity models for fluid transport in jointed rock. J. Geophys. Res. Solid Earth 100 (B12), 24611–24627. https://doi.org/10.1029/95JB02161.

Biot, M.A., 1962. Mechanics of deformation and acoustic propagation in porous media. J. Appl. Phys. 33 (4), 1482–1498. https://doi.org/10.1063/1.1728759.

Biot, M.A., Willis, D.G., 1957. The elastic coefficients of the theory of consolidation. J. Appl. Mech. 24, 594–601. https://doi.org/10.1115/1.4011606.

Budiansky, B., O'Connell, R.J., 1980. Bulk dissipation in heterogenous media. Solid Earth Geophys. Geotechnol. ASME 1–10.

Chen, X.L., Tang, X.M., Qian, Y.P., 2014. Simulation of multipole acoustic logging in cracked porous formations. Geophysics 79 (1), D1–D10. https://doi.org/10.1190/geo2013-0163.1.

Deng, W., Morozov, I.B., 2019. Macroscopic mechanical properties of porous rock with one saturating fluid. Geophysics 84 (6), MR223–MR239. https://doi.org/10.1190/geo2018-0602.1.

Deng, W., Morozov, I.B., 2020. A simple and general macroscopic model for local-deformation effects in fluid-saturated porous rock. Geophys. J. Int. 220 (3), 1893–1903. https://doi.org/10.1093/gji/ggz552.

Dvorkin, J., Mavko, G., Nur, A., 1995. Squirt flow in fully saturated rocks. Geophysics 60 (1), 97–107. https://doi.org/10.1190/1.1443767.

Dvorkin, J., Nur, A., 1993. Dynamic poroelasticity: a unified model with the squirt and the Biot mechanisms. Geophysics 58 (4), 524–533. https://doi.org/10.1190/1.1443435.

Engelder, T., Lash, G.G., Uzcátegui, R.S., 2009. Joint sets that enhance production from middle and upper devonian gas shales of the appalachian basin. AAPG Bull. 93 (7), 857–889. https://doi.org/10.1306/03230908032.

Foldy, L.L., 1945. The multiple scattering of waves. I. General theory of isotropic scattering by randomly distributed scatterers. Phys. Rev. 67 (3–4), 107–119. https://doi.org/10.1103/PhysRev.67.107.

Fu, B.Y., Fu, L.Y., Guo, J., et al., 2020. Semi-analytical solution to the problem of frequency dependent anisotropy of porous media with an aligned set of slit cracks. Int. J. Eng. Sci. 147. https://doi.org/10.1016/j.ijengsci.2019.103209.

Fu, B.Y., Guo, J., Fu, L.Y., et al., 2018. Seismic dispersion and attenuation in saturated porous rock with aligned slit cracks. J. Geophys. Res. Solid Earth 123 (8), 6890–6910. https://doi.org/10.1029/2018JB015918.

Galvin, R.J., Gurevich, B., 2007. Scattering of a longitudinal wave by a circular crack in a fluid-saturated porous medium. Int. J. Solid Struct. 44 (22–23), 7389–7398. https://doi.org/10.1016/j.ijsolstr.2007.04.011.

Galvin, R.J., Gurevich, B., 2009. Effective properties of a poroelastic medium containing a distribution of aligned cracks. J. Geophys. Res. Solid Earth 114 (B7). https://doi.org/10.1029/2008JB006032.

Golsanami, N., Sun, J., Liu, Y., et al., 2019. Distinguishing fractures from matrix pores based on the practical application of rock physics inversion and NMR data: a case study from an unconventional coal reservoir in China. J. Nat. Gas Sci. Eng. 65, 145–167. https://doi.org/10.1016/j.jngse.2019.03.006.

Gassmann, F., 1951. Elastic waves through a packing of spheres. Geophysics 16 (4), 673–685. https://doi.org/10.1190/1.1437718.

Gudmundsson, A., 2011. Rock Fractures in Geological Processes. Cambridge University Press.

Guo, J., Gurevich, B., 2020a. Effects of coupling between wave-induced fluid flow and elastic scattering on P-wave dispersion and attenuation in rocks with aligned fractures. J. Geophys. Res. Solid Earth 125 (3), e2019JB018685. https://doi.org/10.1029/2019JB018685.

Guo, J., Gurevich, B., 2020b. Frequency-dependent P wave anisotropy due to wave-induced fluid flow and elastic scattering in a fluid-saturated porous medium with aligned fractures. J. Geophys. Res. Solid Earth 125 (8), e2020JB020320. https://doi.org/10.1029/2020JB020320.

Guo, J., Gurevich, B., Chen, X., 2022b. Dynamic SV-wave signatures of fluid-saturated porous rocks containing intersecting fractures. J. Geophys. Res. Solid Earth 127 (8), e2022JB024745. https://doi.org/10.1029/2022JB024745.

Guo, J., Rubino, J.G., Barbosa, N.D., et al., 2018a. Seismic dispersion and attenuation in saturated porous rocks with aligned fractures of finite thickness: theory and numerical simulations—Part 1: P-wave perpendicular to the fracture plane. Geophysics 83 (1), WA49–WA62. https://doi.org/10.1190/geo2017-0065.1.

Guo, J., Rubino, J.G., Barbosa, N.D., et al., 2018b. Seismic dispersion and attenuation in saturated porous rocks with aligned fractures of finite thickness: theory and numerical simulations—Part 2: frequency-dependent anisotropy. Geophysics 83 (1), WA63–WA71. https://doi.org/10.1190/geo2017-0066.1.

Guo, J., Shuai, D., Wei, J., et al., 2018c. P-wave dispersion and attenuation due to scattering by aligned fluid saturated fractures with finite thickness: theory and experiment. Geophys. J. Int. 215 (3), 2114–2133. https://doi.org/10.1093/gji/ggy406.

Guo, J., Zhao, L., Chen, X., et al., 2022a. Theoretical modelling of seismic dispersion, attenuation and frequency-dependent anisotropy in a fluid-saturated porous rock with intersecting fractures. Geophys. J. Int. 230 (1), 580–606. https://doi.org/10.1093/gji/ggac070.

Gurevich, B., Makarynska, D., de Paula, O.B., et al., 2010. A simple model for squirt-flow dispersion and attenuation in fluid-saturated granular rocks. Geophysics 75 (6), N109–N120. https://doi.org/10.1190/1.3509782.

Gurevich, B., Zyrianov, V.B., Lopatnikov, S.L., 1997. Seismic attenuation in finely layered porous rocks: effects of fluid flow and scattering. Geophysics 62 (1), 319–324. https://doi.org/10.1190/1.1444133.

Hill, R., 1965. A self-consistent mechanics of composite materials. J. Mech. Phys. Solid. 13 (4), 213–222. https://doi.org/10.1016/0022-5096(65)90010-4.

Hudson, J.A., 1981. Wave speeds and attenuation of elastic waves in material containing cracks. Geophys. J. Int. 64 (1), 133–150. https://doi.org/10.1111/j.1365-246X.1981.tb02662.x.

Ivars, D.M., Pierce, M.E., Darcel, C., et al., 2011. The synthetic rock mass approach for jointed rock mass modelling. Int. J. Rock Mech. Min. Sci. 48 (2), 219–244. https://doi.org/10.1016/j.ijrmms.2010.11.014.

Jiang, Y., Li, B., Yamashita, Y., 2009. Simulation of cracking near a large underground cavern in a discontinuous rock mass using the expanded distinct element method. Int. J. Rock Mech. Min. Sci. 46 (1), 97–106. https://doi.org/10.1016/j.ijrmms.2008.05.004.

Johnson, D.L., Koplik, J., Dashen, R., 1987. Theory of dynamic permeability and tortuosity in fluid-saturated porous media. J. Fluid Mech. 176, 379–402. https://doi.org/10.1017/S0022112087000727.

Johnston, D.H., Toksöz, M.N., Timur, A., 1979. Attenuation of seismic waves in dry and saturated rocks: II. Mechanisms. Geophysics 44 (4), 691–711. https://doi.org/10.1190/1.1440970.

Kuster, G.T., Toksöz, M.N., 1974. Velocity and attenuation of seismic waves in two-phase media: Part I. Theoretical formulations. Geophysics 39 (5), 587–606. https://doi.org/10.1190/1.1440450.

Liu, C., Mehrabian, A., Abousleiman, Y.N., 2017a. Poroelastic dual-porosity/dual-permeability after-closure pressure-curves analysis in hydraulic fracturing. SPE J. 22 (1), 198–218. https://doi.org/10.2118/181748-PA.

Liu, C., Zhang, R., Zhang, H., et al., 2017b. Genesis and reservoir significance of multi-scale natural fractures in Kuqa foreland thrust belt, Tarim Basin, NW China. Petrol. Explor. Dev. 44 (3), 495–504. https://doi.org/10.1016/S1876-3804(17)30057-5.

Ma, R., Ba, J., 2020. Coda and intrinsic attenuations from ultrasonic measurements in tight siltstones. J. Geophys. Res. Solid Earth 125 (4), e2019JB018825. https://doi.org/10.1029/2019JB018825.

Markova, I., Ronquillo Jarillo, G., Markov, M., et al., 2014. Squirt flow influence on sonic log parameters. Geophys. J. Int. 196 (2), 1082–1091. https://doi.org/10.1093/gji/ggt442.

Mavko, G., Mukerji, T., Dvorkin, J., 2020. The Rock Physics Handbook. Cambridge university press.

Nelson, R., 2001. Geologic Analysis of Naturally Fractured Reservoirs, second ed. Gulf Professional Publishing, Oxford, UK.

Noble, B., 1963. The solution of Bessel function dual integral equations by a multiplying-factor method. Math. Proc. Camb. Phil. Soc. 59, 351–362. https://doi.org/10.1017/S0305004100036987.

O'Connell, R.J., Budiansky, B., 1974. Seismic velocities in dry and saturated cracked solids. J. Geophys. Res. 79 (35), 5412–5426. https://doi.org/10.1029/JB079i035p05412.

O'Connell, R.J., Budiansky, B., 1977. Viscoelastic properties of fluid-saturated cracked solids. J. Geophys. Res. 82 (36), 5719–5735. https://doi.org/10.1029/JB082i036p05719.

Pride, S.R., Berryman, J.G., 2003a. Linear dynamics of double-porosity dual-permeability materials. I. Governing equations and acoustic attenuation. Phys. Rev. 68 (3), 036603. https://doi.org/10.1103/PhysRevE.68.036603.

Pride, S.R., Berryman, J.G., 2003b. Linear dynamics of double-porosity dual-permeability materials. II. Fluid transport equations. Phys. Rev. 68 (3), 036604. https://doi.org/10.1103/PhysRevE.68.036604.

Pride, S.R., Berryman, J.G., Harris, J.M., 2004. Seismic attenuation due to wave-induced flow. J. Geophys. Res. Solid Earth 109 (B1). https://doi.org/10.1029/2003JB002639.

Sato, H., Fehler, M.C., Maeda, T., 2012. Seismic Wave Propagation and Scattering in the Heterogeneous Earth. Springer Science & Business Media.

Shang, J., West, L.J., Hencher, S.R., et al., 2018. Geological discontinuity persistence: implications and quantification. Eng. Geol. 241, 41–54. https://doi.org/10.1016/j.enggeo.2018.05.010.

Sherief, H.H., El-Maghraby, N.M., 2003. An internal penny-shaped crack in an infinite thermoelastic solid. J. Therm. Stresses 26 (4), 333–352. https://doi.org/10.1080/713855898.

Song, Y., 2017. Dynamic-equivalent Model of Heterogeneous Porous Media and Longitudinal Wave Scattering by a Permeable Crack in a Porous Medium. Ph.D. thesis. Harbin Institute of Technology (in Chinese).

Song, Y., Hu, H., Rudnicki, J.W., 2017. Dynamic stress intensity factor (Mode I) of a permeable penny-shaped crack in a fluid-saturated poroelastic solid. Int. J. Solid Struct. 110, 127–136. https://doi.org/10.1016/j.ijsolstr.2017.01.034.

Song, Y., Rudnicki, J.W., Hu, H., et al., 2020. Dynamics anisotropy in a porous solid

with aligned slit fractures. J. Mech. Phys. Solid. 137, 103865. https://doi.org/10.1016/j.jmps.2020.103865.
Song, Y., Wang, J., Hu, H., et al., 2021. Frequency-dependent anisotropy in porous rocks with aligned cracks containing compressible fluid—a model based on poroelastic spring condition and exact solution of scattering by a circular crack at oblique incidence. Geophys. J. Int. 226 (2), 1105–1129. https://doi.org/10.1093/gji/ggab145.
Tang, X.M., Cheng, C.H.A., 2004. Quantitative Borehole Acoustic Methods, vol. 24. Elsevier.
Tang, X.M., Chen, X.L., Xu, X.K., 2012. A cracked porous medium elastic wave theory and its application to interpreting acoustic data from tight formations. Geophysics 77 (6), D245–D252. https://doi.org/10.1190/geo2012-0091.1.
Tillotson, P., Chapman, M., Sothcott, J., et al., 2014. Pore fluid viscosity effects on P- and S-wave anisotropy in synthetic silica-cemented sandstone with aligned fractures. Geophys. Prospect. 62 (6), 1238–1252. https://doi.org/10.1111/1365-2478.12194.
Thomsen, L., 1985. Biot-consistent elastic moduli of porous rocks: low-frequency limit. Geophysics 50 (12), 2797–2807. https://doi.org/10.1190/1.1441900.
Walsh, J.B., 1965. The effect of cracks on the compressibility of rock. J. Geophys. Res. 70 (2), 381–389. https://doi.org/10.1029/JZ070i002p00381.
Wang, H.M., Tang, X.M., 2021. Inversion of dry and saturated P-and S-wave velocities for the pore-aspect-ratio spectrum using a cracked porous medium elastic wave theory. Geophysics 86 (6), A57–A62. https://doi.org/10.1190/geo2021-0071.1.
Wu, T.T., 1966. The effect of inclusion shape on the elastic moduli of a two-phase material. Int. J. Solid Struct. 2 (1), 1–8. https://doi.org/10.1016/0020-7683(66)90002-3.
Yao, Q., Han, D.H., Yan, F., et al., 2015. Modeling attenuation and dispersion in porous heterogeneous rocks with dynamic fluid modulus. Geophysics 80 (3), D183–D194. https://doi.org/10.1190/geo2013-0410.1.
Zhang, C., Gross, D., 1993. Wave attenuation and dispersion in randomly cracked solids—II. Penny-shaped cracks. Int. J. Eng. Sci. 31 (6), 859–872. https://doi.org/10.1016/0020-7225(93)90098-F.
Zhang, L., Ba, J., Carcione, J.M., 2021. Wave propagation in infinituple-porosity media. J. Geophys. Res. Solid Earth 126 (4), e2020JB021266. https://doi.org/10.1029/2020JB021266.
Zhang, L., Ba, J., Carcione, J.M., et al., 2019. Modeling wave propagation in cracked porous media with penny-shaped inclusions. Geophysics 84 (4), WA141–WA151. https://doi.org/10.1190/geo2018-0487.1.
Zhang, L., Ba, J., Carcione, J.M., et al., 2022. Seismic wave propagation in partially saturated rocks with a fractal distribution of fluid-patch size. J. Geophys. Res. Solid Earth 127 (2), e2021JB023809. https://doi.org/10.1029/2021JB023809.